2023

OPTIMIZING THE EXTRUDABILITY OF 6082 ALUMINUM BY VARYING THE MAGNESIUM AND SILICON CONCENTRATION

Eli A. Harma
Michigan Technological University, eaharma@mtu.edu

OPTIMIZING THE EXTRUDABILITY OF 6082 ALUMINUM BY VARYING THE MAGNESIUM AND SILICON CONCENTRATION

By

Eli A. Harma

A THESIS

Submitted in partial fulfillment of the requirements for the degree of

MASTER OF SCIENCE

In Materials Science and Engineering

MICHIGAN TECHNOLOGICAL UNIVERSITY

2023

This thesis has been approved in partial fulfillment of the requirements for the Degree of MASTER OF SCIENCE in Materials Science and Engineering.

Department of Materials Science and Engineering

Thesis Advisor:	*Dr. Paul Sanders*
Committee Member:	*Dr. Walter Milligan*
Committee Member:	*Dr. Stephen Kampe*
Committee Member:	*Dr. David Labyak*
Committee Member:	*Dr. Douglas Swenson*
Department Chair:	*Dr. Walter Milligan*

Table of Contents

Acknowledgments

Getting to where I am now has been a great journey and several people have helped me along the way. I would like to give thanks to everyone who has contributed to my education as I could not have done it without them. I am thankful for the encouragement from my family, especially my parents who supported me throughout my education thus far and encouraged me to go to graduate school. I would not be able to be where I am without the help and lessons, they have given me over the years.

In terms of the research performed in this paper several people and organizations have contributed towards the completion of this research. The first group I would like to thank is Relativity Space whose funding helped pay for the experiments performed. I would also like to thank the Michigan Tech ACMAL group whose laboratories I used to perform several analyses over the duration of this project.

Next, I would like to acknowledge my advisor Dr. Paul Sanders who has guided me throughout the duration of this project and has given me invaluable feedback. He has also done a significant amount to further my education by teaching me how to properly report and present my findings.

I also must give thanks to the research engineers that work for the Materials Science and Engineering department including Tow Wood, Russ Stien, Dr. Dale Dewald, and Paul Fraley. I would like to give extra thanks to Tom Wood for his expertise in aluminum and aluminum extrusion, which was invaluable. Many discussions with Tom helped further the project and helped me when I was stuck.

The last group of people I would like to acknowledge are my fellow graduate students in the MSE department. Working with the other graduate students, including brainstorming, and helping with their projects has been great. I am especially grateful for my office mate Isabella who has been part of invaluable brainstorming sessions and assisted me with my EBSD analysis.

Abstract

Alloy 6082 aluminum is used for high-volume manufacturing in the automotive industry due to its high strength, impact performance, and corrosion resistance. However, given these improved properties, the alloy has decreased formability compared to other 6xxx series alloys, especially in the extrusion process. Controlling the dynamic recovery and recrystallization properties by changing the additions of Mg and Si can improve the hot deformation properties. Five alloys of varying Mg and Si concentrations between 0.6 to 1.2wt% Mg and 0.7 to 1.3wt% Si were made with constant concentrations of Cr, Fe, and Mn and the same homogenization heat treatment. The proposed alloys are tested using hot compression to identify the activation energy for hot deformation at temperatures of 400℃, 450℃, and 500℃ with strain rates of $0.1s^{-1}$, $0.01s^{-1}$, and $0.001s^{-1}$. The resulting compression samples are analyzed using EBSD to identify the fraction recrystallized. The results show that increasing Mg from 0.6 to 1.2wt% decreases the activation energy from 262 to 220 kJ/mol. In contrast, increases in Si from 0.7 to 1.3wt% decreased the recrystallization fraction and increased activation energy from 262 to 292 kJ/mol. An optimal composition range was identified to be a ratio of Mg to Si between 0.8 and 1, as all alloys close to this ratio had low recrystallized fractions and activation energies compared to other alloys tested for the select temperature and strain rate conditions.

1.0 Introduction and Overview

6xxx series alloys are employed in the automotive industry for their high yield strength, ductility, corrosion resistance, and formability. An alloy used for high-volume production is 6082, which has higher strength and improved crash performance compared to other 6xxx series alloys [1]. The increased properties are linked to the higher levels of Mg and Si (Figure 1) and the addition of Cr, Fe, and Mn, which form dispersoids [1]. The addition of dispersoids reduces recrystallization during extrusion and produce a fine grain structure responsible for the elevated yield and impact strength [2]. These enhanced properties make 6082 desirable for use in bumpers, frame rails, and crash cans, all components which require higher strength and toughness for crash performance [3]. An undesirable property of 6082 is the decrease in formability during extrusion caused by elevated high-temperature flow stress due to the Mg, Si, and dispersoid concentrations [4]. As extrusion is used to make several components in automobiles, identifying methods for improving the extrusion properties will make 6082 more economical for manufacturing.

Common methods to improve extrusion performance include optimizing the homogenization heat treatment and altering the chemical composition [2]. These factors influence dispersoid formation and the amount of solute in solution leading to changes in the high-temperature flow stress [2]. Given the known benefits of dispersoids, any modifications to the alloy must not eliminate dispersoid-forming elements. Therefore, identifying which microstructural characteristic affects hot deformation is critical for optimizing extrusion while having limited effects on the final profile properties. This research will assess how changing concentrations of Mg, and Si alloying additions affect

the mechanical properties and the dynamic recovery and recrystallization response of a 6082 alloy given a constant thermal processing condition and Cr, Fe, and Mn content.

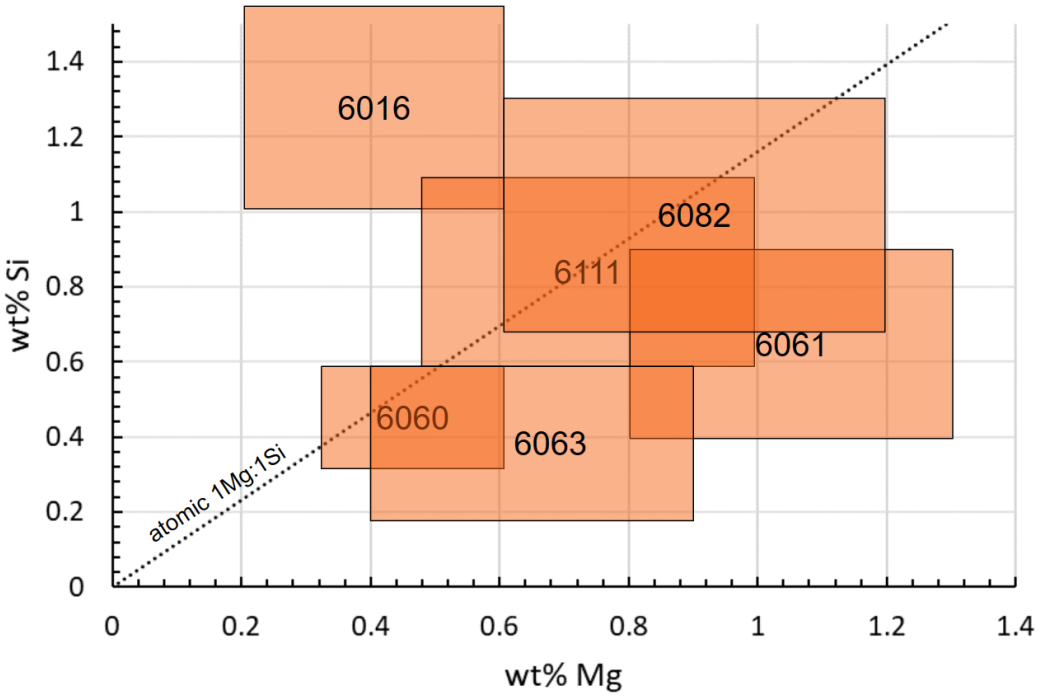

Figure 1. The compositional limits for Mg and Si of several other 6xxx series alloys [5].

1.1.1 Basics of Aluminum Extrusion

The most common extrusion process is direct extrusion, as it requires less intricate tooling and can be performed easily on a large scale [6]. In direct extrusion, a billet is pushed with a ram through a container into an extrusion die (Figure 2). The material plastically flows through the extrusion die, forming a final extrusion geometry dictated by the die shape. Hot deformation occurs in the region between the ram end and the beginning of the die. Here strain rates will vary from 0.1 s^{-1} to a maximum of 100 s^{-1}, and temperatures exceed half of the melting point ($T > 0.5T_m$). Important metrics for the quality of the extrusion process are the breakthrough pressure, denoted as the maximum

pressure reached, and the steady state flow region (Figure 2) [7]. The pressure in the steady state region is not constant but steadily decreases throughout the process due to a reduction in billet length, which reduces frictional forces. However, the pressure in the region can be related to the high-temperature flow stress of the material in which lower values correspond with lower pressures at breakthrough and the steady-state region. The flow stress and, therefore, pressure are also significantly affected by temperature and strain rate. Higher temperatures require lower pressures to deform the billet, while higher speeds increase the pressure for deformation. Therefore, any modification to the alloy that lowers the extrusion pressure and increases the extrusion velocity improves direct extrusion productivity. Improved productivity enables companies to manufacture a higher volume of extruded aluminum in less time, lowering production costs.

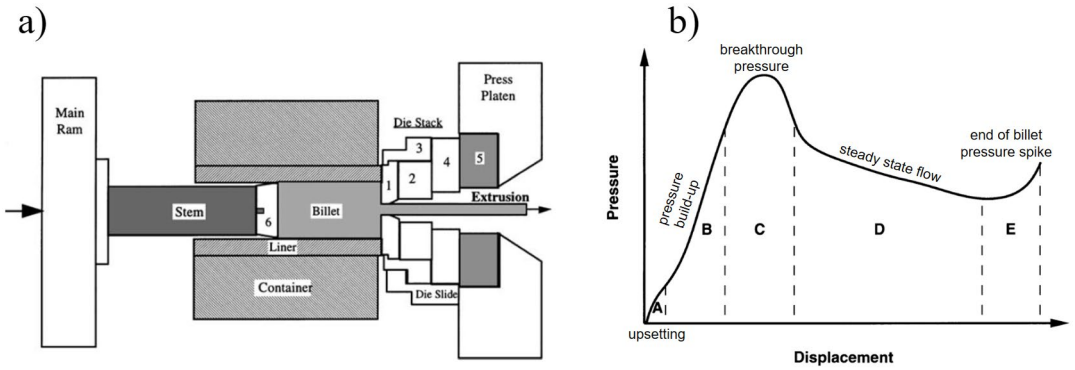

Figure 2. a) Typical direct extrusion system schematic with labeled associated components. b) The pressure v. displacement graph for the direct extrusion process where (A) is the upsetting process, (B) is the pressure build-up, (C) breakthrough pressure, (D) is the steady state flow region, and (E) is the end of billet pressure increase [6].

The thermal cycle for the extrusion process starts with casting the billet using the direct chill process or steel molding (Figure 3). The direct chill process directly cools the billet with water as it is cast, while steel molding cools in the billet air. The next step in the process is homogenization at a temperature of around 450°C - 550°C, which is held to

ensure a homogeneous distribution of solute and growth of dispersoids [8]. Once cooled, the billet is reheated for extrusion temperatures using a rapid heating source to avoid the formation of Mg_2Si and extruded. After extrusion, the profile must be quenched with water at the die exit to stop the precipitation of Mg_2Si. The extruded profile is then aged to precipitate the Mg_2Si and strengthen the material.

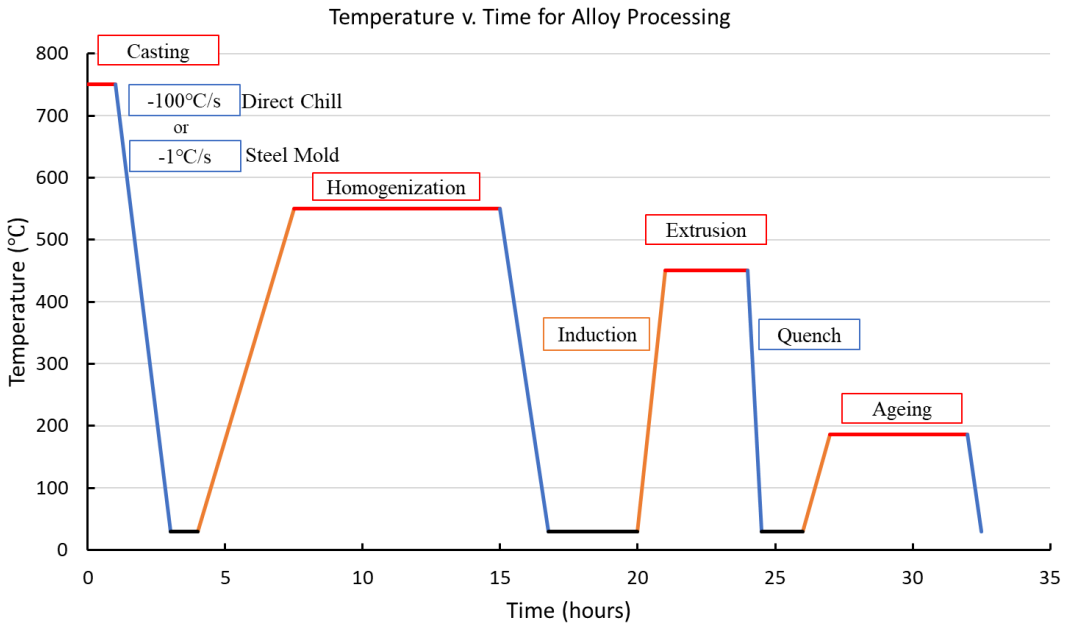

Figure 3. Time v. temperature graphic for the extrusion of a 6xxx series billet beginning from casting to the final aging process.

1.2 6082 Alloying Additions and Homogenization

1.2.1 Overview of 6082

The 6082 alloy is 98% aluminum with Mg, Si, Cr, Cu, Mn, and Fe additions or impurities (Table 1). The chemistry ranges allotted for 6082 allow for the manipulation of the composition to improve the properties during and after extrusion. The additions of Si, Cr, Fe, and Mn are essential for the formation of dispersoids which aid in reducing the

amount of recrystallization in the alloy during extrusion and after the subsequent aging heat treatment [9]. The formation of these dispersoids increases the strength compared to other 6xxx series alloys and makes the alloy less formable. Adding Cu also notably increases the yield strength but is limited to 0.1 wt% due to decreased corrosion resistance [7]. The main additions of Mg and Si also allow for significant improvements to the mechanical properties, given the formation of the Mg_2Si precipitate phase and solid solution strengthening.

Table 1. The ASTM B221-21 specification for aluminum alloy compositions for extruded bars, rods, wire, profiles, and tubes in wt% [10].

Alloy	Si	Fe	Cu	Mn	Mg	Cr	Zn	Ti
6082	0.7-1.3	0.5 max	0.1 max	0.4-1.0	0.6-1.2	0.25 max	0.2 max	0.1 max

1.2.2 Mg and Si in the 6082 alloy

Magnesium and silicon are the primary additions of the 6xxx series alloy system. The 6082 alloy has the highest range of Mg 0.6 to 1.2wt% and Si 0.7 to 1.3wt% of all 6xxx series alloys, enabling significant alterations to its mechanical properties by changing these concentrations (Figure 1). The magnesium and silicon additions have high solubility in aluminum (Figure 4). The pseudo-binary phase diagram of Al-Mg_2Si shows that at a temperature of 550°C, there is a maximum solubility of 1.5 wt% Mg_2Si in aluminum [11]. This means that Mg up to 3 wt% and Si up to 1.5 wt% will dissolve into a solid solution at a homogenization temperature of 550°C for the ternary system. However, since there are inclusions that contain concentrations of Cr, Mn, and Fe some of the Si is used to form them while the remainder is a solid solution. Therefore, Mg and Si additions can significantly impact the material's dynamic recovery and

recrystallization properties due to solid solution strengthening present after homogenization.

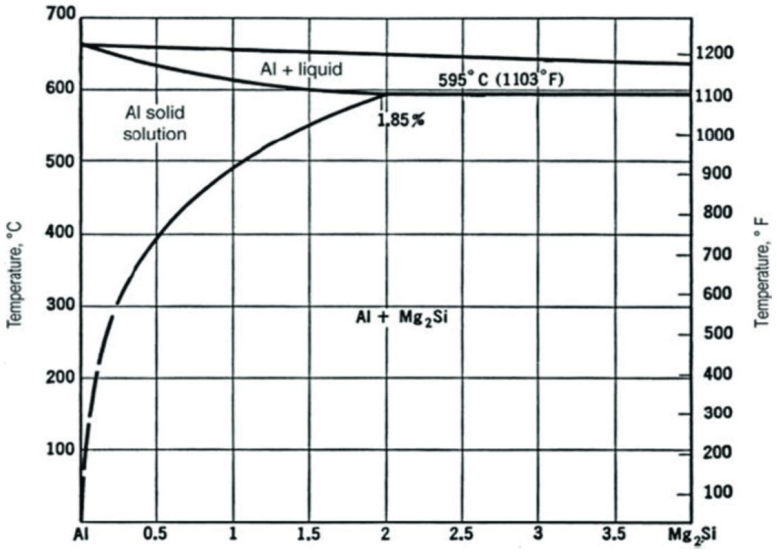

Figure 4. The Al-Mg_2Si pseudo-binary phase diagram. The bottom axis is in wt% Mg_2Si [11].

The ratios of Mg and Si in the 6xxx series can also have a significant effect on the type of precipitate formed during homogenization cooling and after extrusion. Precipitation will begin to occur at temperatures more than 200℃, beginning with a supersaturated solid solution and following the precipitation sequence starting with the formation of GP zones. After the formation of the GP zones needle-like **β**"(Mg_5Si_6) structure forms, then the rod-like **β**'(Mg_5Si_6) phase, and finally, the **β**(Mg_2Si) phase (Figure 5) [12]. It is important to note that the Mg_5Si_6 is a metastable structure and can be present in the final structure after homogenization and aging. Considering the two possible Mg and Si precipitates it should be noted that each has a different ratio of Mg to Si when considering their mass fraction, for Mg_5Si_6 the ratio is 0.72, and for Mg_2Si the ratio is 1.73. This means for the 6082 range of magnesium and silicon various ratios are possible when considering the limits (Table 2). Each of the limits has a Mg/Si ratio which

is like that of the Mg_5Si_6 ratio where the only alloy which is close to the Mg_2Si ratio is the 1.2 wt% Mg and 0.7 wt% Si composition. Given these ratios it is possible that metastable Mg_5Si_6 is present in all combinations of Mg and Si.

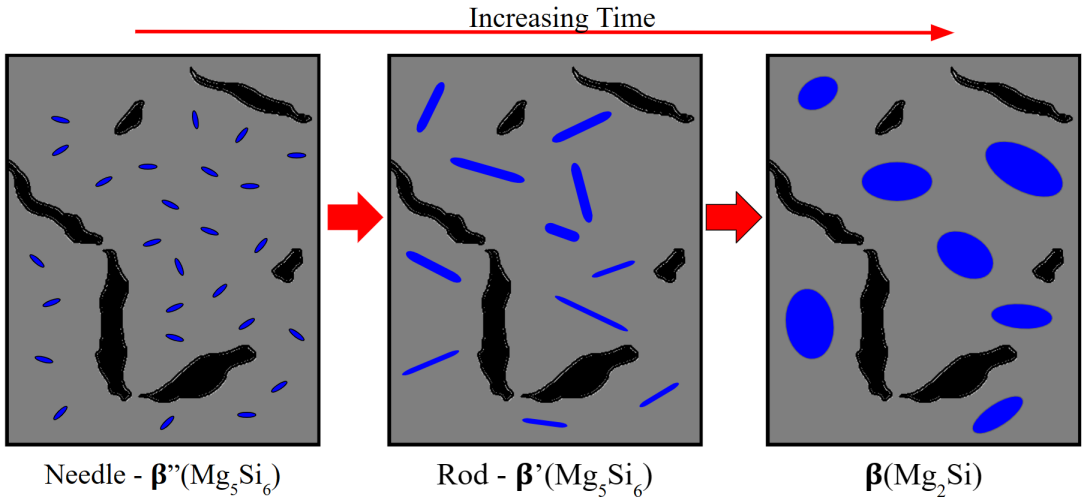

Figure 5. Precipitation sequence of the Mg_2Si phase skipping the GP zone formation at a temperature of around 200°C given a supersaturated solid solution [13].

Table 2. Ratio of the wt% Mg to the wt% of Si for the compositional limits of 6082 including the center point.

Mg	Si	Ratio Mg / Si
0.6	0.7	0.86
1.2	0.7	1.71
0.6	1.3	0.46
0.9	1.0	0.9
1.2	1.3	0.92

1.2.3 Dispersoid Forming Elements in the 6082 Alloy

The Cr, Mn, Si, and Fe additions in 6082 are responsible for forming dispersoids in the alloy after casting and the homogenization process (Figure 6). Dispersoids formed include the and **β**-Al_5FeSi and the **α**-$Al_{12}(FeMnCr)_3Si$ precipitates which form near grain boundaries creating a precipitate free zone [14]. The **β**-Al_5FeSi dispersoid forms during casting and has a monoclinic crystal structure and needle like morphology [15]. The **β**-

Al_5FeSi dispersoid then transforms to the **α**-$Al_{12}(FeMnCr)_3Si$ structure during subsequent homogenization. The transformation takes place at temperatures greater than 500°C where the Cr and Mn can diffuse to the dispersoids. The transformed **α**-$Al_{12}(FeMnCr)_3Si$ dispersoid has a body centered cubic structure and a rounded morphology [8]. This dispersoid is incoherent with the microstructure and has been found to have an average effective diameter of 74 ± 20 nm [16].

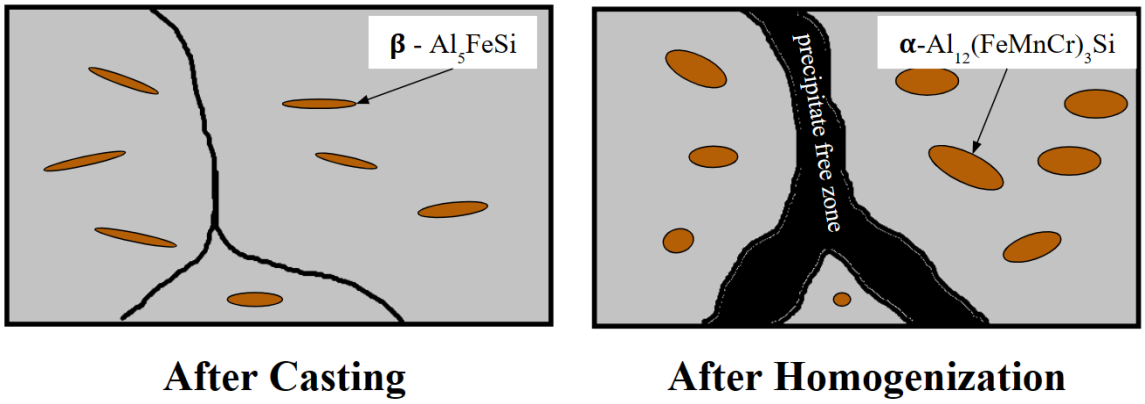

Figure 6. The change in microstructure after casting and the subsequent homogenization heat treatment. Highlighted are the transformation of the **β**-Al_5FeSi dispersoid to the **α**-$Al_{12}(FeMnCr)_3Si$ chemistry and rounded morphology.

1.2.4 Homogenization of the 6082 Extrusion Alloy

Homogenization is a crucial step used to improve extrusion and final properties of the profile due to the redistribution of solute through the matrix and dispersoid formation. The process also affects the microstructure by changing the as cast dendritic structure to equiaxed, shrinking the interdendritic region, and creating a precipitate-free zone at the grain boundaries [9].

The **β**-Al_5FeSi dispersoid is formed during solidification preferentially near interdendritic regions (Figure 6). After casting and during homogenization the **β**-Al_5FeSi will transform to the spherical **α**-$Al_{12}(FeMnCr)_3Si$ dispersoid via diffusion of Cr and Mn

[17]. To aid in transforming the **β**-Al_5FeSi and forming new **α**-$Al_{12}(FeMnCr)_3Si$ slower heating rates around 100-200°C/hr are used to aid in homogeneous nucleation of the dispersoids throughout the microstructure [11]. Times greater than 10 hours and temperatures greater than 550°C for homogenization do lead to coarsening of the dispersoid [17].

The final factor influenced by the homogenization heat treatment is the formation of Mg_2Si during the cooling step. Research has identified a link between cooling rate and decreased extrusion pressure and yield strength of the extruded profiles. The consensus is that slower cooling rates after homogenization will increase the volume fraction and size of Mg_2Si, which forms in the microstructure [15]. The larger sizes and higher volume fractions of the Mg_2Si precipitates do not completely dissolve during extrusion and have been linked with lower extrusion pressure. However, coarse Mg_2Si precipitates have been linked to incipient melting and therefore hot tearing of the extrusion at high temperatures and extrusion speeds [7]. The larger precipitates are also detrimental to the final properties of the extruded profile, which rely on a subsequent aging heat treatment after extrusion to attain peak properties.

Optimal homogenization conditions aim to transform all **β**-Al_5FeSi to the rounded **α**-$Al_{12}(FeMnCr)_3Si$ and control the size and volume fraction of Mg_2Si. To obtain this microstructure the homogenization must use a heating rate between 100-200°C/hr to the homogenization temperature, hold at a temperature between 450-550°C for 6-8hr, and cool at a rate between 300-600°C/hr (Figure 7). If these metrics are achieved, the extrusion properties of the alloy will be optimized by control of the hot deformation mechanisms through alloying of Mg and Si.

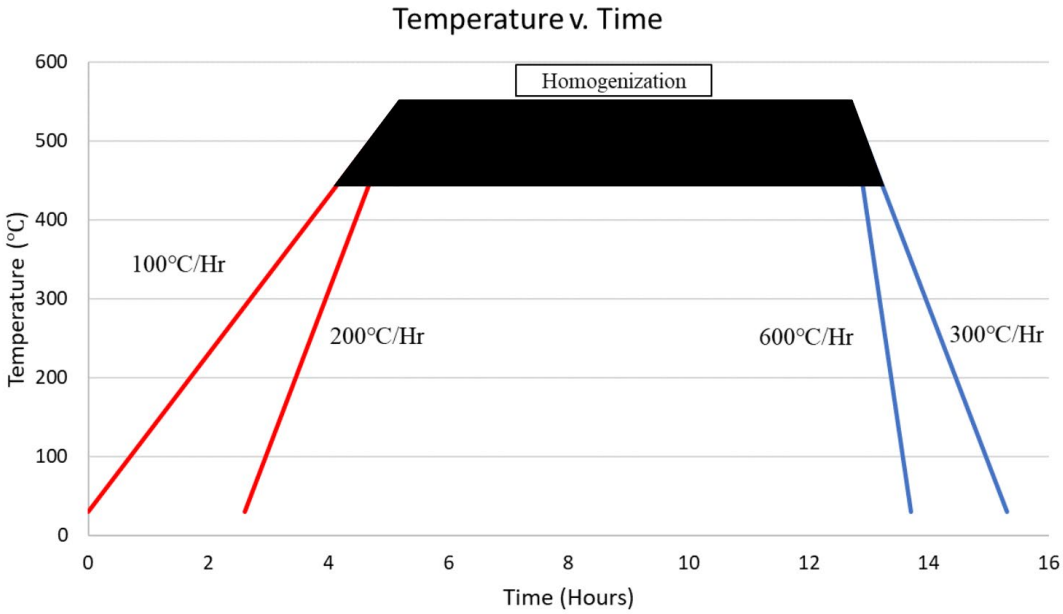

Figure 7. Optimal homogenization time v. temperature graph for 6xxx series aluminum where the heating rates range between 100-200°C/hr (red), homogenization temperature ranges between 450-550°C (black), and the cooling rates range between 300-600°C/hr (blue) [15].

1.3 Previous Research Performed on 6082 Alloys

Previous research has been performed on 6082 to look at various aspects of the alloy including the effect of different homogenizations and alloying additions on the hot deformation properties. No research has been conducted to target the optimal composition of Mg and Si in 6082 for improved extrusion properties. However, some research has been conducted on pure Al-Mg-Si alloys and the effects of Mg and Si on the extrusion properties which is insightful. New research is required to look at the effects of Mg and Si additions to the hot deformation activation energy and recrystallization properties of the 6082 alloy.

Research Schiffl et al. looked at different alloying additions and homogenization conditions for 6082 aluminum to identify which parameter most influenced high temperature flow stress. He showed that the homogenization condition, Mn concentration and Cr continent had the most significant influence on the high temperature flow stress [2]. The researchers were not able to identify which high temperature deformation mechanism these factors affected and why there was an increase in the high temperature flow stress. Linking the change in the high temperature flow stress to the hot deformation activation energy and deformation mechanism is important for targeting an optimal composition as these characteristics can be directly related to extrusion performance.

Other researchers have looked at the sole effect of dispersoids containing Mn, Cr, and Fe on the hot deformation activation energy and recrystallization properties in 6xxx series alloys [18], [19]. Wang et al. identified that the addition of Cr and Mn to a 6061 alloy increased the dispersoids density which significantly increased the activation energy for hot deformation and reduced the amount of recrystallization [18]. He however did not include the effects of increasing Mg and Si concentration on these properties. As it is known that Si is a major contributor to dispersoid formation, understanding how Si concentration affects dispersoid formation will be important.

Some research has been performed on the effect of Mg and Si in alloys without dispersoid forming elements on the extrusion performance [4],[20],[21]. Odoh found that an increase in Mg and Si for a 6xxx series alloy had a significant increase to the high temperature flow stress and an increase to the activation energy for hot defromation [4]. He was also able to conclude that increasing Mg and Si concentration reduced the extrusion velocity by 50%. The research however did not investigate the effects of

additions such as Mn and Fe which are crucial for 6082 and or how the Mg and Si content would affect the recrystallization properties.

Given these findings, there exists a need to explore how Mg and Si affect the hot deformation of 6082 to optimize the alloy for extrusion. As inclusion of Cr, Fe, and Mn are required for the improved impact resistance optimization must them. Optimization must also look to control the amount of recrystallization as high amounts will negatively impact the performance of the 6082 aluminum.

1.4 Hot Deformation Mechanisms of Extrusion

1.4.1 Review of Dynamic Recovery and Recrystallization

Two main mechanisms lower the flow stress during extrusion: dynamic recovery and dynamic recrystallization. During the strain hardening process, plastic strain is applied, which causes dislocations to form and propagate through the material, continuously increasing stress due to increased dislocation densities. At elevated temperatures, dynamic recovery, and recrystallization act to lower this stress caused by increased dislocation densities. Dynamic recovery is the first process that occurs directly at the onset of strain hardening. A reduction in flow stress occurs due to the decrease in dislocation density caused by the annihilation of dislocation and the formation of subgrains at elevated temperatures. Dynamic recovery will continue to lower the flow stress of the material until the hardening and softening process reaches a point of equilibrium, indicated by a plateau in flow stress to a steady state (Figure 8) [22].

The next form of softening is dynamic recrystallization which, unlike recovery, is initiated when the material's strain hits a critical amount at the peak in flow stress. Softening will occur via the nucleation and growth of new grains, decreasing dislocations' density and, therefore, the flow stress. The stress will then steadily decrease to a steady state value limited by the strain rate and temperature (Figure 8). The decrease in flow stress for the recrystallization process combines both dynamic recovery and recrystallization affects as the dynamic recovery occurs at all stages of the strain-hardening process.

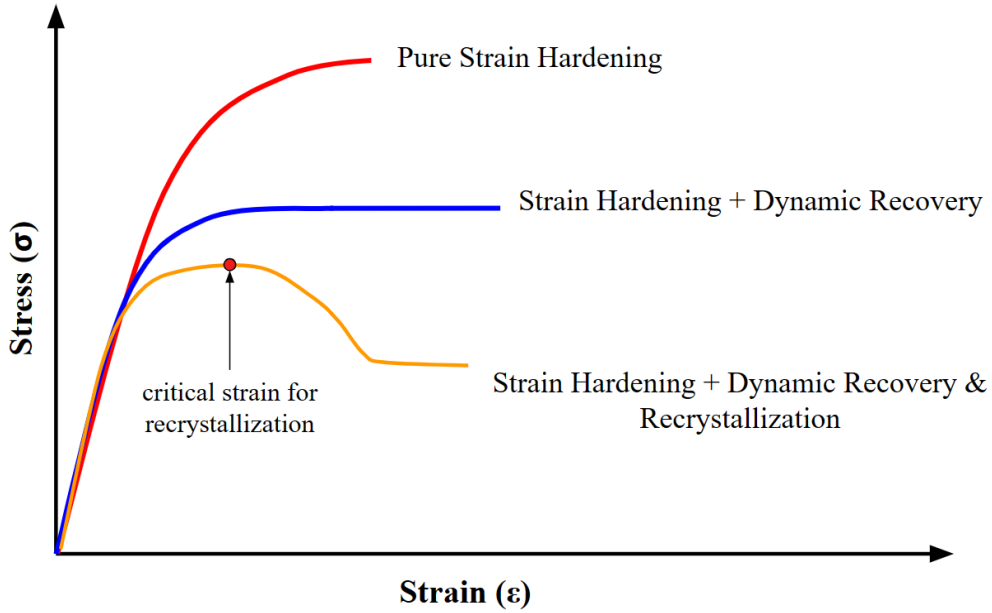

Figure 8. A stress versus strain plot showing the general effect of the dynamic recovery and recrystallization processes on a polycrystalline metal's pure strain hardening properties during compression testing [23].

It is typical in aluminum extrusion alloys to have combinations of dynamic recovery and recrystallization. However, aluminum's high stacking fault energy compared to other alloys yields higher fractions of dynamic recovery [24]. Therefore, any additions of solute, precipitates, and/or dispersoids which increase the resistance for

dynamic recovery or decrease the stacking fault energy will dampen the effects of dynamic recovery and cause more dynamic recrystallization. Identifying which factors most influence the recovery mechanism is essential for optimizing the high-temperature deformation properties. One way of identifying these effects is by identifying the activation energy for hot deformation, which is directly related to the energy barrier required for dislocations to propagate through a material. Therefore, lower activation energies will indicate more recrystallization while higher activation energies will indicate more dynamic recovery. This is because the recrystallization process decreases dislocation densities faster than dynamic recovery after the critical strain is reached.

1.4.2 Inverse Hyperbolic Sine Model

Due to the complexity of the dynamic recovery and recrystallization process, no mechanistic models independently capture the effect of solute, precipitate, and or dispersoid strengthening. However, the inverse hyperbolic sine model, which is a constitutive relationship, can be used to measure the activation energy of hot deformation. Since the activation energy is independent of temperature and strain rate; therefore, it can be used as a metric to predict which mechanism of hot deformation is more active.

The inverse hyperbolic sine law accesses the activation energy for hot deformation by using the Zener-Hollomon relationship (Equation 1), where $\dot{\varepsilon}$ is the strain rate, Q is the activation energy for hot deformation, R is the gas constant, and T is the temperature. The activation energy for extrusion purposes is derived by measuring the flow stress of a material under compression or torsion at multiple strain rates and

temperatures. The activation energy is calculated using (Equation 2) where $\boldsymbol{\sigma}$ is the steady state flow stress, $\boldsymbol{\alpha}=\boldsymbol{\beta}/n_1$, and the values of n, n_1, $\boldsymbol{\beta}$, and S are derived from the average of the slopes of ln(έ) vs. ln[sinh($\boldsymbol{\alpha\sigma}$)], ln(έ) vs. ln($\boldsymbol{\sigma}$), ln(έ) vs. $\boldsymbol{\sigma}$, ln[sinh($\boldsymbol{\alpha\sigma}$)] vs. 1/T respectively (Table 3) [25].

$$Z = \acute{\varepsilon}\, exp\left(\frac{Q}{RT}\right) \qquad \text{Equation 1.}$$

$$Q = R * \acute{\varepsilon} * \left[\frac{\partial ln(\varepsilon)}{\partial ln[sinh(\alpha\sigma)]}\right]_T * \left[\frac{\partial ln[sinh(\alpha\sigma)]}{\partial(1/T)}\right] \quad \text{Equation 2.}$$

Table 3. Variable for the inverse hyperbolic sine model and the associated equations used to fit. Note that έ is the strain rate, $\boldsymbol{\sigma}$ is the true stress, and T is the temperature.

Variable	Fitting Slopes
n_1	ln(έ) vs. ln($\boldsymbol{\sigma}$)
$\boldsymbol{\beta}$	ln(έ) vs. $\boldsymbol{\sigma}$
$\boldsymbol{\alpha}$	$\boldsymbol{\beta}/n_1$
n	ln(έ) vs. ln[sinh($\boldsymbol{\alpha\sigma}$)]
S	ln[sinh($\boldsymbol{\alpha\sigma}$)] vs. 1/T

The activation energy Q is then related to the high-temperature flow stress through the hyperbolic sine function (Equation 3), where A is a material constant. Equation 3. then simplifies to (Equation 4), which shows the dependence of the steady-state flow stress σ with the Zener-Holloman parameter Z [26].

$$Z = A(sinh(\alpha\sigma))^n \qquad \text{Equation 3.}$$

$$\sigma = \frac{1}{\alpha} sinh^{-1}\left[\left(\frac{Z}{A}\right)^{\frac{1}{n}}\right] \qquad \text{Equation 4.}$$

The high-temperature flow stress and Zener-Holloman parameter depend on temperature and strain rate. Higher temperatures and slow strain rates coincide with lower Zener-Holloman values and flow stresses with an associated increase in recrystallization fraction (Figure 9). While higher strain rates and lower temperatures correspond with a higher Zener-Holloman value and flow stress with a decrease in the fraction of recrystallization (Figure 9). So, at a constant temperature and strain rate, lower values for the activation energy will correspond with lower flow stress and increased fractions of recrystallization.

To measure the activation energy multiple strain rates and temperatures are used to quantify the activation energy meaning lots of data is collected in this form of analysis. One method for comparing the results includes analyzing data at Zener-Hollomon values which are at the high ln(Z) having a temperature of 400℃ and strain rate 0.1 s^{-1}, a medium ln(Z) having a temperature of 450°C and strain rate 0.01 s^{-1}, and a low ln(Z) condition having a temperature of 500℃ and strain rate 0.001 s^{-1} (Figure 9). Significant differences between these three conditions make it easy to compare variables such as the flow stress and recrystallization for different materials. It should be noted that the high ln(Z) condition will have the least amount of recrystallization while the low ln(Z) conditions will have the most.

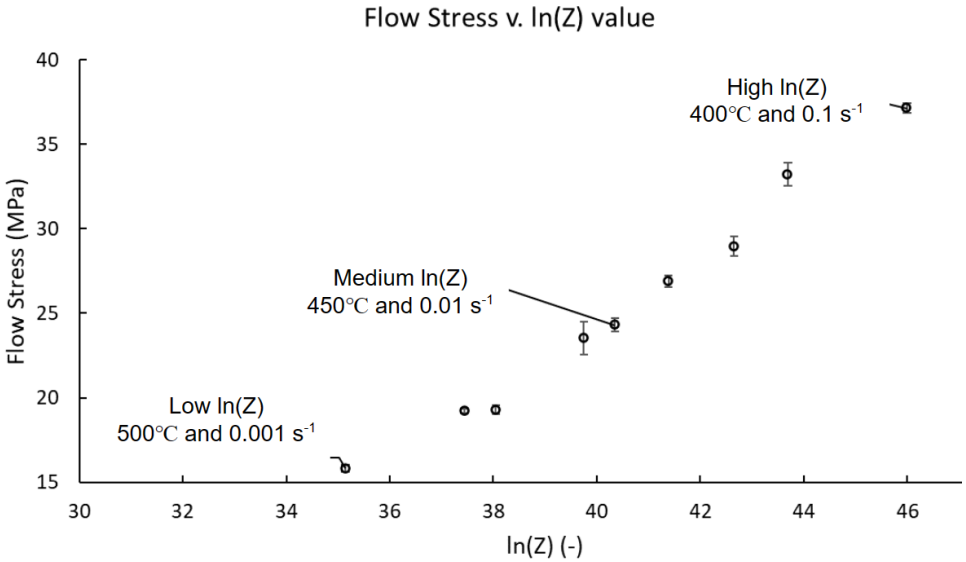

Figure 9. The Flow Stress v. ln(Z) condition for the tested low Mg and high Si alloy. Highlighted are the high ln(Z) condition of 400℃ and 0.1 s^{-1}, the medium ln(Z) condition of 450℃ and 0.01 s^{-1} and low ln(Z) condition of 500℃ and 0.001 s^{-1}.

1.5 The Effect of Microstructure on Hot Deformation

1.5.1 The Effect of Solute and Precipitates on Hot Deformation in 6xxx Series Alloys

In Al-Mg-Si alloys, the intermetallic precipitate phase Mg_2Si is present before extrusion but will mostly dissolve during billet preheating. To understand the effects of this phase, researchers have looked at the effects of cooling rate after homogenization on the flow stress. For example, Zajac et al. analyzed the 6005 extrusion alloy at a water quench rate and a slow cool rate of 40°C/hr to precipitate Mg_2Si in different volume fractions and sizes [27]. The slowest cooling rate produced the highest volume fraction and largest radius of Mg_2Si, while the quench produced none. The measured flow stress of 6005 alloy after the slow cool was lower than after quenching at every deformation temperature (Figure 10). Since the slow cool had an increase in Mg_2Si precipitates it is

concluded that the precipitate provides a smaller increase to the flow stress than the solid solution.

An increased fraction of Mg_2Si present in the final microstructure also affected the flow stress of the alloy as the temperature increased. As can be seen, increasing temperature decreased the change between the quench and slow cool conditions (Figure 10). As the temperature increases, the decreased delta between these two conditions is caused by dissolving more amounts of Mg_2Si into solid solution. The increased solute concentration in the slow cool alloy decreased the observable change in flow stress as the temperature increased.

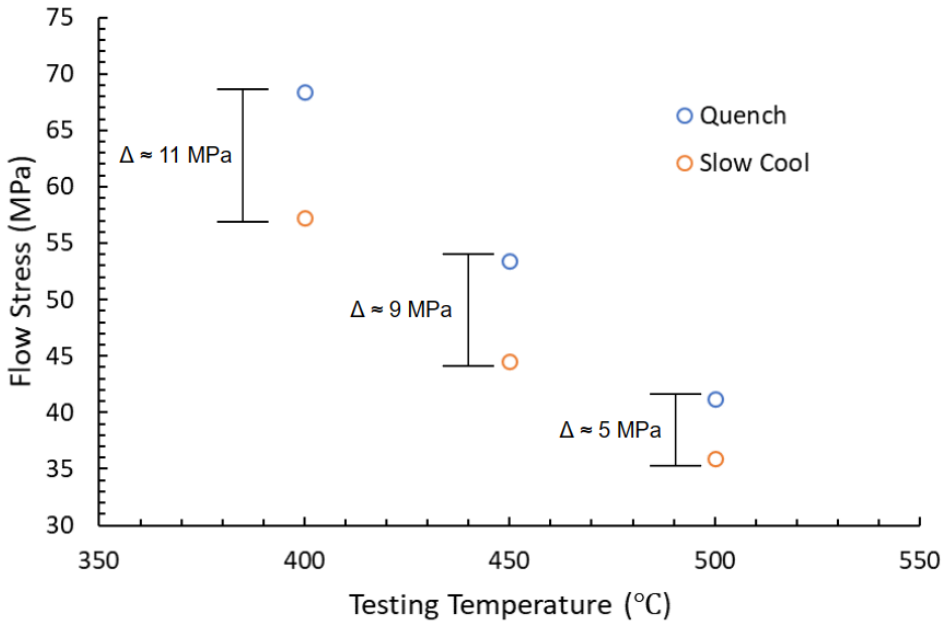

Figure 10. The flow stress of the 6005 versus the deformation temperature of the three different homogenization cooling conditions. The difference between the quench condition and the 40°C/hr cooling rate is noted [27].

1.5.2 The Effect of Dispersoids on the Hot Deformation of 6xxx Series Alloys

The needle shaped **β**-Al_5FeSi dispersoid forms in 6082 alloys after casting and transforms to the rounded **α**-$Al_{12}(FeMnCr)_3Si$. The **β**-Al_5FeSi is an undesirable dispersoid that forms in the microstructure and can be eliminated by controlling the concentration of Fe and Mn. It has been found that the **β**-Al_5FeSi dispersoid are not formed in the alloy due to the inclusion of Mn, which causes the preferential formation of the **α**-$Al_{12}(FeMnCr)_3Si$ dispersoid when the concentration of Fe is below 1 wt%, and the concentration of Mn is greater than 0.5 wt% [8].

The **α**-$Al_{12}(FeMnCr)_3Si$ dispersoid increases the high-temperature flow stress and hot deformation activation energy. An increased concentration of dispersoids has been linked to an increased activation energy and reduced recrystallization fraction. Wang et al. looked at the effect of the **α**-$Al_{12}(FeMnCr)_3Si$ dispersoid on changes to the activation energy for the hot deformation of an Al-Mg-Si alloy. The presence of the **α**-$Al_{12}(FeMnCr)_3Si$ dispersoid increased the activation energy of hot deformation from 148 kJ/mol to 189 kJ/mol [18]. The increase in activation energy was accompanied by an increase in flow stress and a reduced fraction of recrystallization.

Other researchers have looked to understand how the quantity of dispersoids affects the recrystallization properties and flow stress of a 6082 alloy. Nes et al. used an increasing Mn concentration to produce a higher number density of dispersoids in the 6082 alloy. The researchers found that increasing the concentration of Mn in a 6082 alloy from 0.0 to 0.5 wt% reduced the percentage of grain boundaries that were greater than 15° from 50% to 30% (Figure 11) [28]. This indicated that there was a significant

reduction in the amount of recrystallization. The change in Mn concentration also had a significant increase in the flow stress for every strain rate condition at a constant testing temperature of 450°C (Figure 11). Concluding that increasing dispersoid densities increase the flow stress and reduce the fraction of high-angle grain boundary, indicating decreased amounts of recrystallization. This effect is caused by Zener pinning, where small dispersoids act to restrict grain boundary motion limiting recrystallization during hot deformation and increasing the flow stress [17]. This effect is however limited as it was identified that increasing concentration of Mn greater than 0.5 wt% did not significantly decrease the fraction of high angle boundaries below 30% even though there is an associated increase in the flow stress.

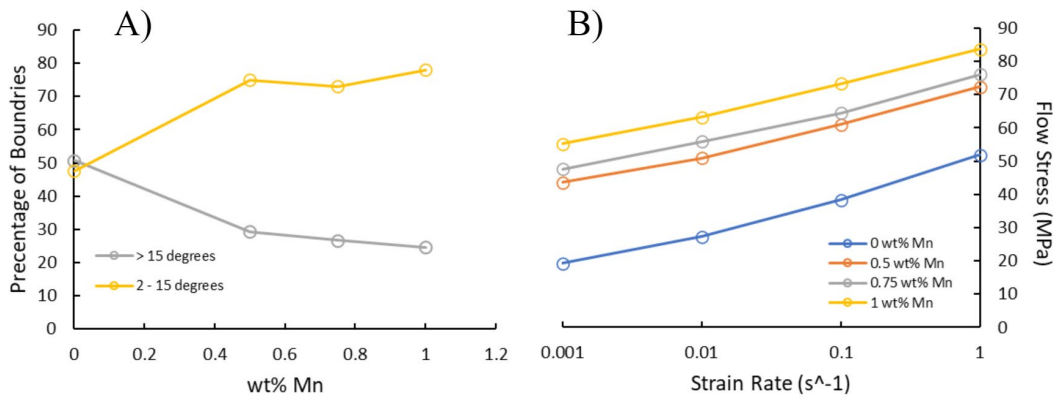

Figure 11. A) The effect of increasing Mn concentration on the fractions of low angle grain boundaries 2° to 15° and high angle grain boundaries >15° for samples tested at a temperature of 500°C and strain rate of $0.01s^{-1}$. B) The flow stress results of four alloys tested at 450°C with increasing strain rates at four compositions of 6082 with increasing amounts of Mn (0 wt%, 0.5 wt%, 0.75 wt%, and 1 wt%) [28].

1.5.3 The Effect of Solid Solution on the Hot Deformation of 6xxx Series Alloys

During extrusion, the Mg_2Si phase dissolves during preheating into the aluminum matrix, increasing the Mg and Si content in solid solution. The increased amount of

solute in the solution increases the hot deformation flow stress of the alloy. This effect is detrimental to the extrusion process as increasing Si and Mg decreases the extrusion velocity (Figure 12). The increase in Mg and Si solute both lower the incipient melting temperature and increase the material's flow stress [29]. Therefore, the increased flow stress caused by solute strengthening requires extrusion at lower temperatures and slower speeds to prevent hot tearing of the material. Which is a negative effect when producing an alloy for optimized production speeds.

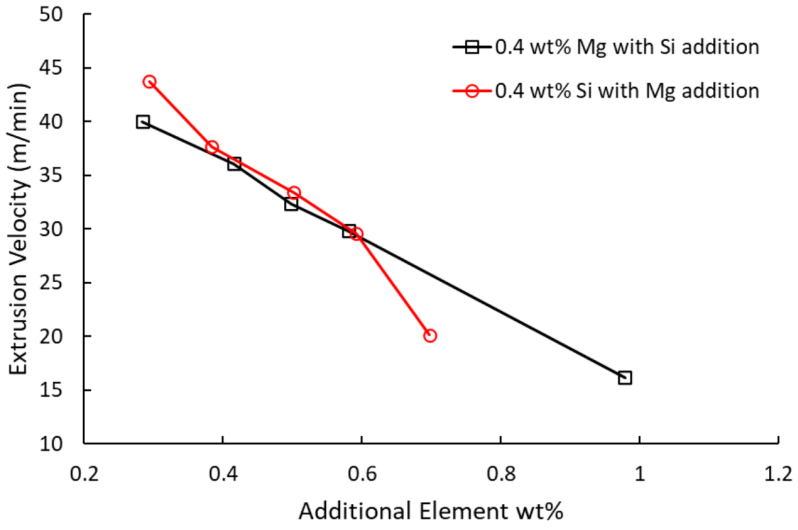

Figure 12. The reduction in extrusion velocity given increase in the wt% Si and wt% Mg present in a 6xxx series alloy given two alloys one with a constant concentration of 0.4 wt% Si and another with 0.4 wt% Mg [30].

The combined effect of Mg and Si in solid solution on the dynamic recovery and recrystallization of aluminum has not been identified, but there is information on the effects of Mg solid solution in aluminum that is applicable. In hot deformation, the annihilation of dislocations is a primary mechanism by which the flow stress decreases during dynamic recovery. If a material has a high stacking fault energy, the dislocation can annihilate via climb, glide, and cross-slip, but at lower stacking fault energies,

dislocation rarely cross-slip and mainly annihilate via climb and glide. The limited cross-slip is caused by the increased distance between partial dislocations, which require more force to slip; therefore, dislocation densities increase [31]. Since the cross-slip of dislocations is linked to increasing dislocation densities in the material, anything which decreases the stacking fault energy will begin to favor the dynamic recrystallization process. Since an increase in Mg solid solution in Al-Mg binary alloys decreases the stacking fault energy of the material [32]. It is believed that the addition of Mg will correspond with an increase in recrystallization.

1.6 Objective and Hypothesis

1.6.1 Objective

The objective of this research is to identify the effect of Mg and Si on the activation energy for hot deformation and the mechanisms of dynamic recovery and recrystallization in 6082. The 6082 alloy will contain the same concentration of Cr, Fe, Mn, and trace elements Ti and Zn. The alloys will be homogenized following the same homogenization treatment for each alloy. Compression testing will be performed at three temperatures and three strain rates to simulate the hot deformation conditions of extrusion.

1.6.2 Hypothesis

If the Mg concentration in 6082 is increased to the high specification limit, then the fraction of low-angle grain boundaries will decrease because the increase in Mg solute will inhibit dynamic recovery and favor recrystallization.

If the Si concentration in 6082 is increased to the high specification limit, then the fraction of low-angle grain boundaries will increase because the increase in Si containing dispersoids will inhibit dynamic recrystallization and favor dynamic recovery.

If the Mg and Si concentrations are both increased in 6082, then the activation energy for hot deformation will increase because increases in solute in solution decrease the stacking fault energy increasing the energy required for dislocation motion.

2.0 Materials and Methods

2.1 Design of Experiments

A further understanding of how the Mg and Si content affect the dynamic recovery and recrystallization mechanisms is required to optimize the 6082 chemistry for extrusion. A design of experiments is proposed to vary the concentration of Mg and Si within the 6082 specification limits while keeping the concentration of Cr, Cu, Fe, and Mn constant with a common homogenization treatment (Table 4), (Table 5). The Mg and Si levels will be varied using two levels of Mg and two levels of Si which are the minimum and maximum of the 6082 ranges (Table 6). A center point will also be used having a composition of 0.9 wt% Mg and 1.0 wt% Si.

Table 4. Elements held constant in 6082 DOE alloys produced for this work (wt%)

Alloy	Cr	Cu	Fe	Mn	Ti	Zn
6082	0.2	0.1	0.25	0.6	< 0.05	< 0.05

Table 5. Homogenization heat treatment for 6082 DOE alloys

Step	Time	Temperature
Heating	3.5 hr	150°C/hr
Homogenization	8 hr	550°C
Cooling	1.75 hr	300°C/hr

Table 6. Two-factor, two-level DOE factor settings

Factor	Level 1	Center Point	Level 2
wt% Mg	0.6	0.9	1.2
wt% Si	0.7	1.0	1.3

2.2 Materials

2.2.1 Casting Method

Alloys were cast at Michigan Technological University using a McEnglevan resistance furnace heated to a superheat of 100℃ above the equilibrium liquidus for each alloy. The furnace used a 12 kg graphite crucible, and the nominal composition was confirmed on a Bruker Q4 Tasman optical emission spectroscopy (OES) utilizing a 6061-type standard. Each heat was degassed with argon for fifteen minutes after the addition of a 20g TiB rod for grain refinement having a maximum of 0.05 wt% Ti (Table 3.). Billets are then cast into a 10 cm diameter x 24 cm cavity length steel mold with the use of a filtered pour cup to form two billets with nominal lengths of 24 cm each (Figure 13).

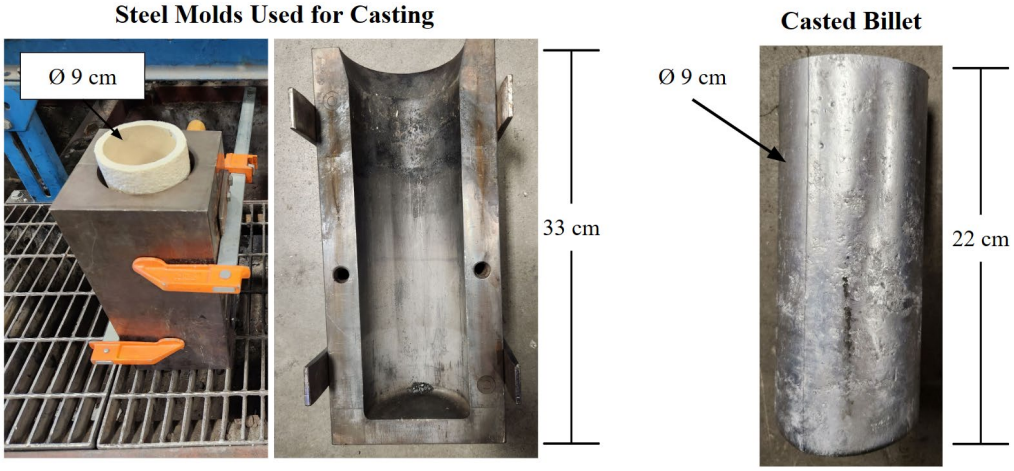

Figure 13. The steel mold used for casting the extrusion billets and an image of the as cast billet.

2.2.2 Homogenization Method

After casting, the alloys were homogenized with the use of a resistant furnace using a PID temperature control system. Homogenization was performed at 550°C for 7.5 hours after the billets reached temperature at a heating rate between 100-150°C/hr. The billets were then cooled at a rate between 250-300 °C/hr until reaching 200°C after which the billets were air cooled to room temperature. The heat treatment was tracked using a thermocouple inserted into the center of the billet to ensure similar homogenization between the different alloys (Figure 14).

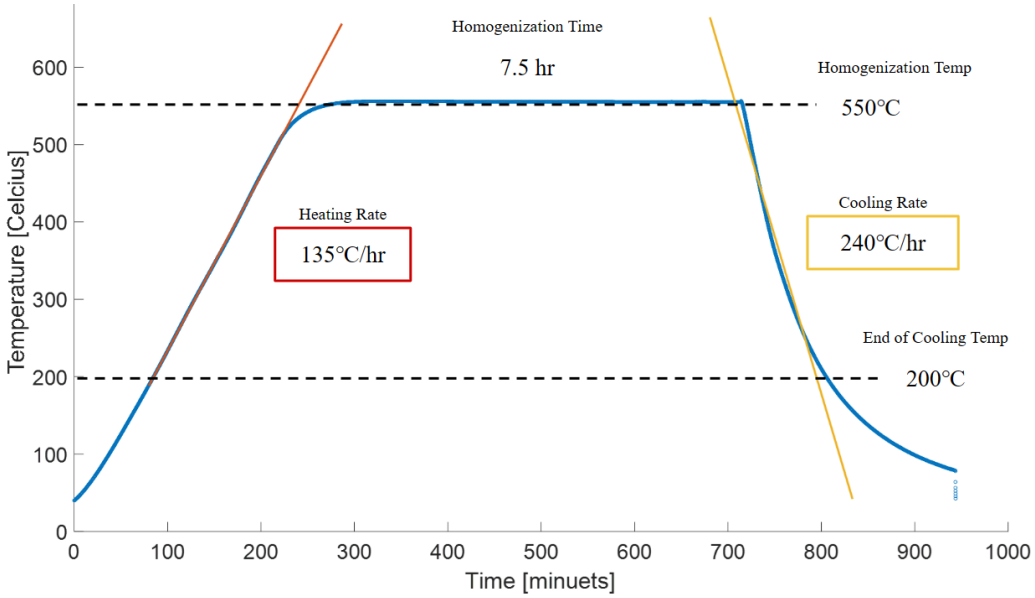

Figure 14. Temperature v. Time profile from the measured homogenization cycle of the low Mg and low Si alloy billet material.

2.3 Sample Preparation

2.3.1 Metallography Samples

Metallography samples were taken from the top section of the billet at the mid-radius (Figure 15). Samples were sectioned and mounted in epoxy and polished to 0.05 µm colloidal silica (Table 7). Samples for SEM analysis were analyzed directly after cleaning with ethanol after the final polishing step (no etching).

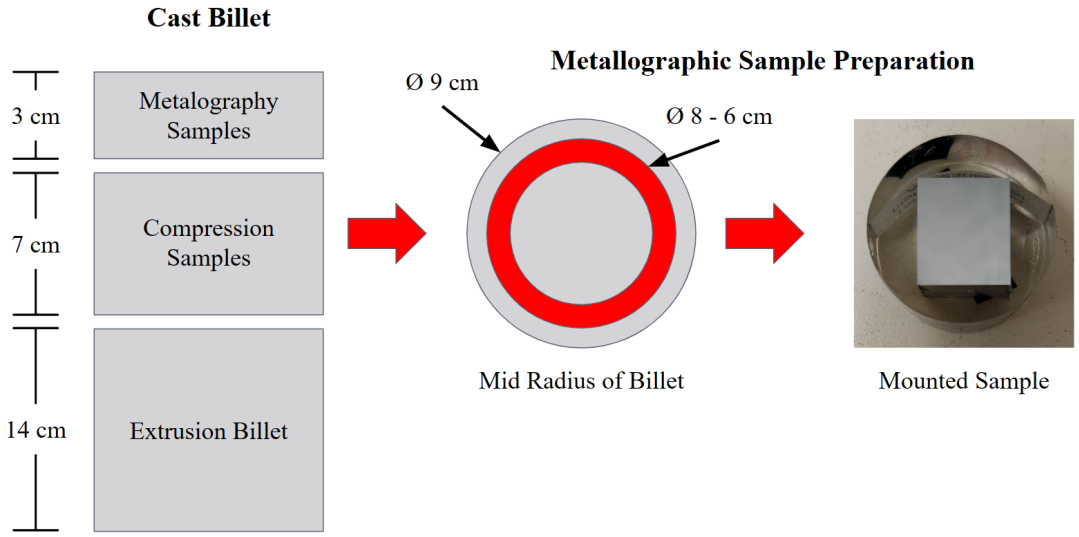

Figure 15. Billet sectioning used to make metallographic samples.

Table 7. Metallographic polishing procedure for all samples used including the as-cast, homogenized, and compressed samples.

Abrasive	Lubricant	Time	Speed	Pressure Setting
240 grit SiC	water	Until flat	200 RPM	hand
500 grit SiC	water	3 minutes	200 RPM	hand
800 grit SiC	water	3 minutes	200 RPM	hand
1200 grit SiC	water	5 minutes	200 RPM	hand
1um diamond Kempad	Red lube	2 minutes	150 RPM	hand
1um diamond Imperial	Red lube	5 minutes	150 RPM	hand
0.05 um colloidal silica	none	3 minutes	100 RPM	hand
Imperial pad	water	30 seconds	100 RPM	hand

2.3.2 Compression Samples

Compression samples cut by wire electro-discharge machining (EDM) from the middle section of the extrusion billet after homogenization. Samples were manufactured in accordance with the ASTM E209-18 standard for samples with 25.4 mm gauge length and 12.7 mm diameter gauge (Figure 16). Lubrication in the form of boron nitride spray was added to the ends of the compression samples before testing.

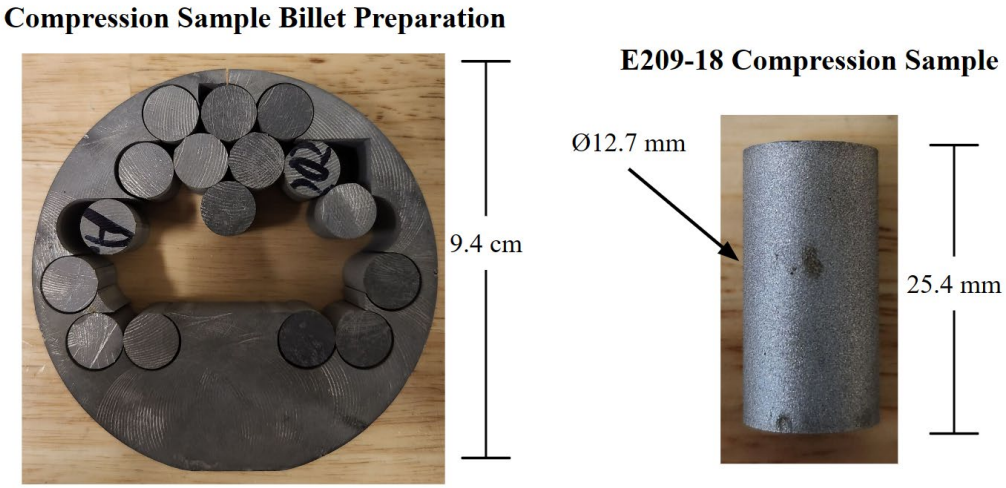

Figure 16. Sample preparation for compression testing including the location of test specimens in the billet and the EDM cut E209-18 compression sample.

2.4 Microstructural Analysis Methods

2.4.1 SEM analysis

Analysis was performed on an FEI Philips XL 40 environmental scanning electron microscope with Oxford instrumentation and AZtec acquisition software for image processing. Images were taken with the use of the backscattered electron detector using an accelerating voltage of 20 kV, a spot size of 6, a working distance of 10 mm, an

image resolution of 1024, and a capture time of 20 seconds (Table 8). For image analysis, the contrast and brightness were adjusted to highlight the interdendritic region and Mg_2Si precipitates in the as cast and homogenized structures. Chemical analysis was also performed with point EDS measurements using an accelerating voltage of 20 kV, a spot size of 6.5, a working distance of 10 mm, and a processing time of 4 seconds.

Table 8. FEI Philips XL 40 ESEM settings for analysis of the microstructure of the samples in as-cast, homogenized, and compressed conditions.

Setting	**Image Analysis Set Value**	**EDS Set Values**
Accelerating Voltage	20 kV	20 kV
Spot Size	6 kV	6.5 kV
Working distance	10 mm	10 mm
Image Resolution	1024	-
Capture Time	20 seconds	-
Processing Time	-	4 seconds

2.4.2 Image Processing

Image processing with ImageJ software was used to identify the fractions of the dendritic region and Mg_2Si present in the as cast and homogenized microstructure of the different alloys. To process the images brightness and contrast of the Mg_2Si and interdendritic region was adjusted to highlight the regions for particle analysis (Figure 17). Given the highlighted regions, particle analysis was performed in ImageJ to identify the total area of the respective phases and the average area of the particles.

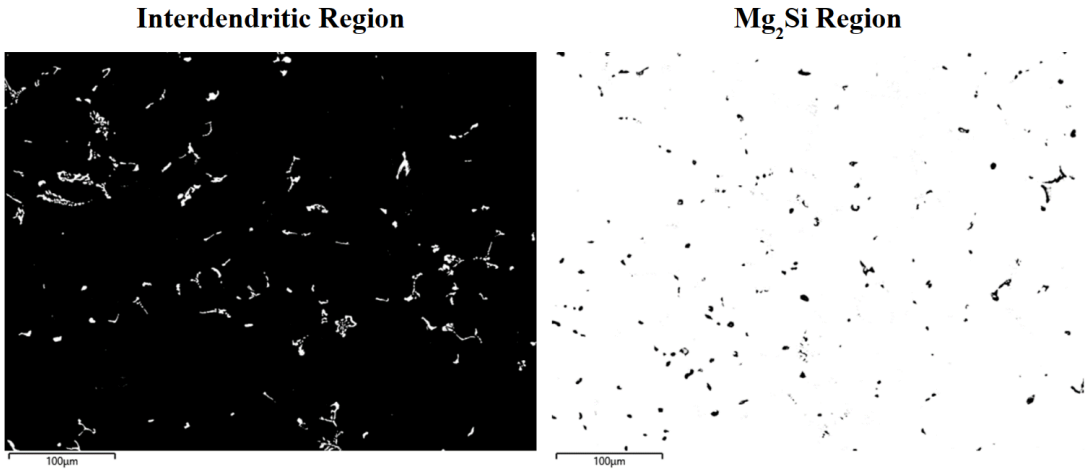

Figure 17. Representation of the two regions for the high Mg and high Si alloy highlighting the interdendritic region and the Mg_2Si phases present in the homogenized condition.

2.4.3 EBSD analysis

Electron backscattered diffraction was performed using an FEI Philips XL 40 environmental scanning electron microscope with Oxford instruments and the AZtec acquisition software for image processing (Table 10). Samples were prepared using cross-sections parallel to the compression directions at the center of the compression sample (Figure 18). Samples where cut using an abrasive saw ground and polished to a final step of 0.05 for 20min to remove residual stresses (Table 9). Two images are taken per alloy for the conditions of 400°C with a strain rate of $0.1s^{-1}$, 450°C with a strain rate of $0.01s^{-1}$, and 500°C with a strain rate of $0.001s^{-1}$. To ensure adequate data acquisition between sample types, data parameters were set to follow the ASTM-E2726 standard with small modification to the maximum number of zero solutions and the minimum number of grains analyzed (Table 11). The average grain misorientation is assessed via the map reconstruction method where each pixel of the EBSD map is analyzed to identify the fraction of high angle boundaries $\theta<15^o$ and low angle boundaries $2^o<\theta<15^o$ [33].

Figure 18. EBSD sample preparation from compressed sample

Table 9. Polishing procedure for all samples used for compressed samples used for EBSD.

Abrasive	Lubricant	Time	Speed
600 grit SiC	water	3 minutes	200 RPM
800 grit SiC	water	3 minutes	200 RPM
1200 grit SiC	water	5 minutes	200 RPM
1um diamond Kempad	Red lube	5 minutes	150 RPM
0.05 um colloidal silica Final-P	none	10 minutes	100 RPM
0.05 um colloidal silica Imperial pad	none	10 minutes	100 RPM
Imperial pad	water	30 seconds	100 RPM

Table 10. ESEM and AZtech software settings used for EBSD analysis.

SEM Model	Accelerating Voltage	Spot Size	Magnification	EBSD Step Size
FEI Philips XL 40	20 kV	6.0	250X	2 µm

Table 11. Methods used for EBSD analysis of average grain misorientations.

	Minimum Average Pixel Resolution Per Grain	Maximum Zero Solution w/o Cleaning	Minimum # of Grain Analyzed
ASTM E2627	100	10%	500
Project Method	100	20%	400

2.5 Mechanical Testing Methods

2.5.1 Hot Compression Testing

Hot compression testing was performed on an Instron 4206 universal test frame with MTS TestSuite TW Elite version 4.5.2.423 software. The system was heated using the Interpower Induction Powerlink 7.0 heating system with PID control. The temperature of the system was controlled via a thermocouple attached to the compression platen and was calibrated at each temperature condition using a sample with embedded thermocouples to assess the temperature at the top, middle, and bottom of the sample before each test batch. The temperature was controlled to a temperature which was ±5°C of the set point with a maximum transient from top to bottom of 10°C. Samples were tested with a 5-minute hold time after achieving the desired temperature setpoint. Tests were performed at three temperatures of 400°C, 450°C, and 500°C, and three test rates of 2.54 mm/s ($0.1s^{-1}$), 0.254 mm/s ($0.01s^{-1}$), and 0.0254 mm/s ($0.001s^{-1}$) to a final engineering compressive strain of 0.6. Three replicates were used for each condition and alloy. The load was measured using a Futek 110kN load cell and extension was measured using crosshead displacement. The resulting load and extension data were collected and processed via MATLAB using equations in Appendix 2. To ensure minimal errors in data collection samples which did not barrel consistently were excluded from the data analysis (Figure 20). The raw flow stress data collected for all materials tested can be found in Appendix 2 (Figure 49 - 53).

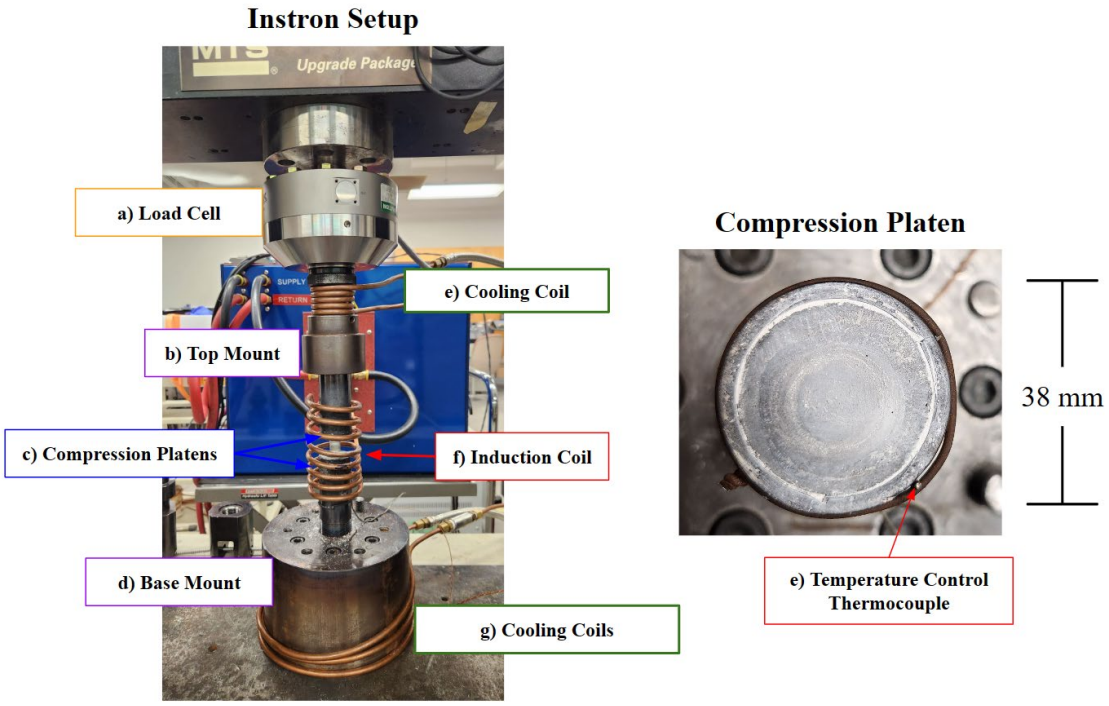

Figure 19. Overall view of the components in the compression testing setup including the a) load cell, b) top mount, c) compression platens, d) base mount, e) cooling coils, f) induction coil, g) base cooling coils, e) temperature control thermocouple.

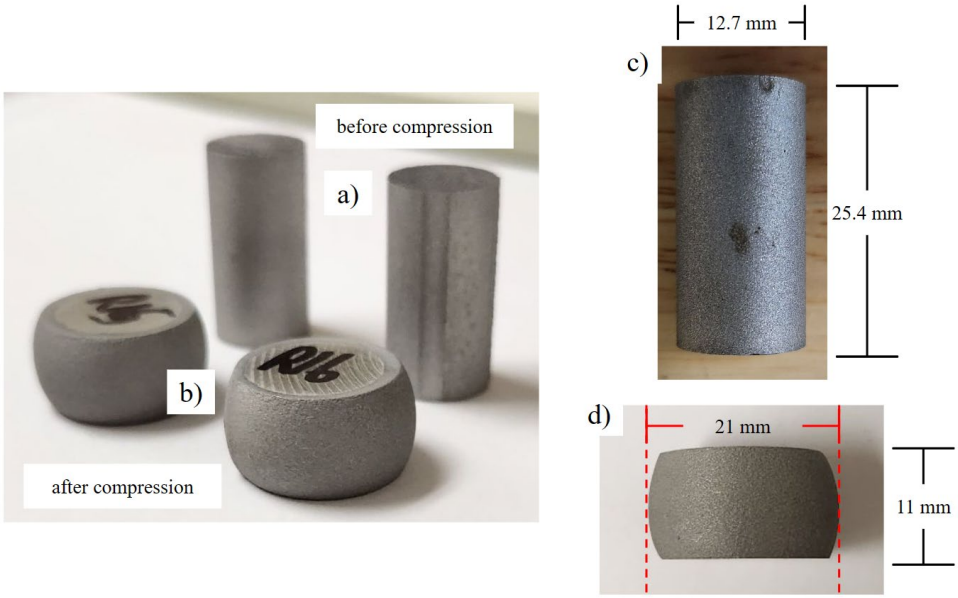

Figure 20. Results of the compression testing analysis a) & c) sample before compression and b) & d) sample after compression.

3.0 Results

3.1 As Cast and Homogenized Microstructure

3.1.1 Cast Chemical Compositions

The five cast alloys have a nominal composition of like the set target (Table 12). The compositions also had an Fe content that has a maximum range of 0.06 wt% from the 0.25wt% target, a Cr content of 0.2 wt% with 0.00 wt% range from the 0.2 wt% target, an Mn content with a maximum of 0.04 wt% range front the 0.6 wt% target, and a Ti and Zn content below the maximum of 0.05 wt% after the addition of the TiB rod.

Table 12. Compositions of the five cast alloys with varying Mg and Si concentrations in wt% balanced with aluminum to a value of 100 wt%.

Alloy	Mg	Si	Fe	Cr	Cu	Mn	Ti	Zn
low Mg & low Si	**0.63**	**0.66**	0.29	0.20	0.08	0.57	0.01	0.01
high Mg & low Si	**1.20**	**0.67**	0.31	0.20	0.08	0.56	0.01	0.01
low Mg & high Si	**0.62**	**1.33**	0.26	0.20	0.08	0.57	0.01	0.01
high Mg & high Si	**1.34**	**1.36**	0.26	0.20	0.08	0.56	0.01	0.01
mid Mg & mid Si	**0.9**	**1.08**	0.29	0.20	0.09	0.57	0.01	0.01

3.1.2 Microstructure

The microstructure of the as cast (Figure 21) and homogenized (Figure 22) alloys had two distinct microconstituents: a white phase which is the intermetallic portion of the interdendritic region and a black phase which is the Mg_2Si . The images do not show any significant porosity from casting. There are also no large Mg_2Si particles, the maximum average particle size is 14 μm^2 per particle, specifically in the high Mg and high Si alloy after homogenization.

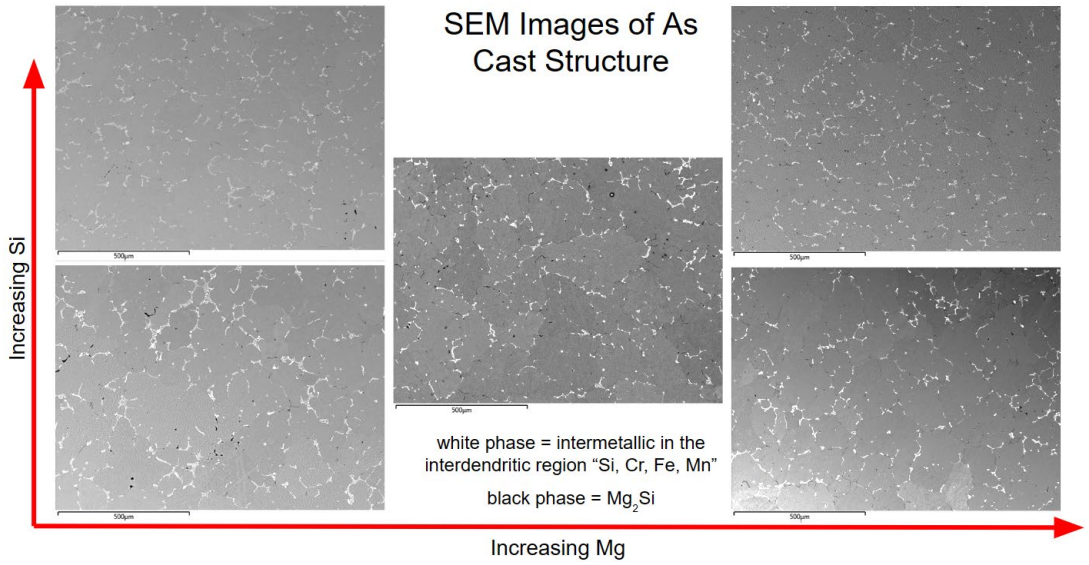

Figure 21. BSE images of the as-cast structure with increasing Mg and Si. The black is the Mg_2Si phase, and the white is the intermetallic in the interdendritic microconstituent.

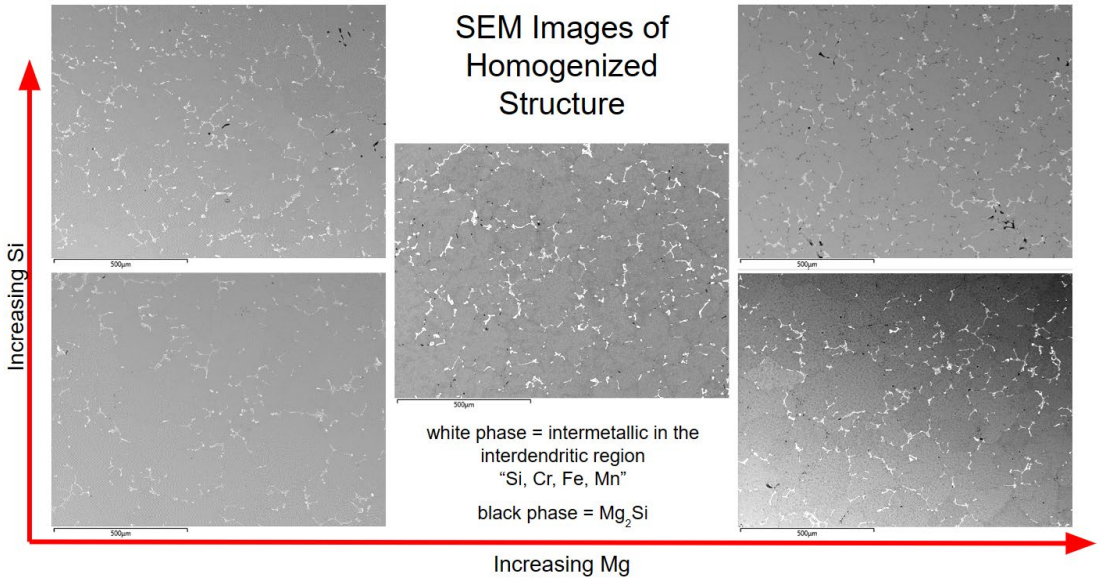

Figure 22. BSE images of the homogenized structure with increasing Mg and Si. The black phase is the Mg_2Si phase, and the white phase is the intermetallic in the interdendritic microconstituent.

3.2 Image Analysis

3.2.1 Area Fraction of Mg_2Si

Image analysis of the as-cast and homogenized 6082 alloys was performed to access the area fraction of Mg_2Si formed during casting and after homogenization (Figure 23). There was a statistically significant increase in average area fraction with increasing Mg and Si. As expected, the homogenization heat treatment generally decreased the average Mg_2Si area fraction for each alloy (Figure 24).

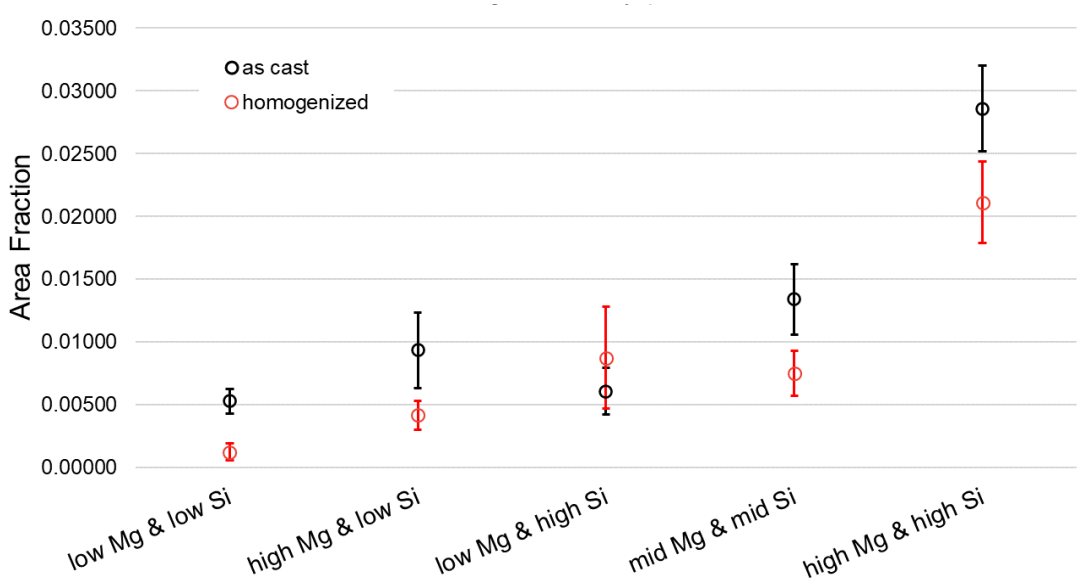

Figure 23. The area fraction of Mg_2Si per alloy type given the homogenized and as-cast condition. Note the error bars are 95% confidence in the standard error of the mean.

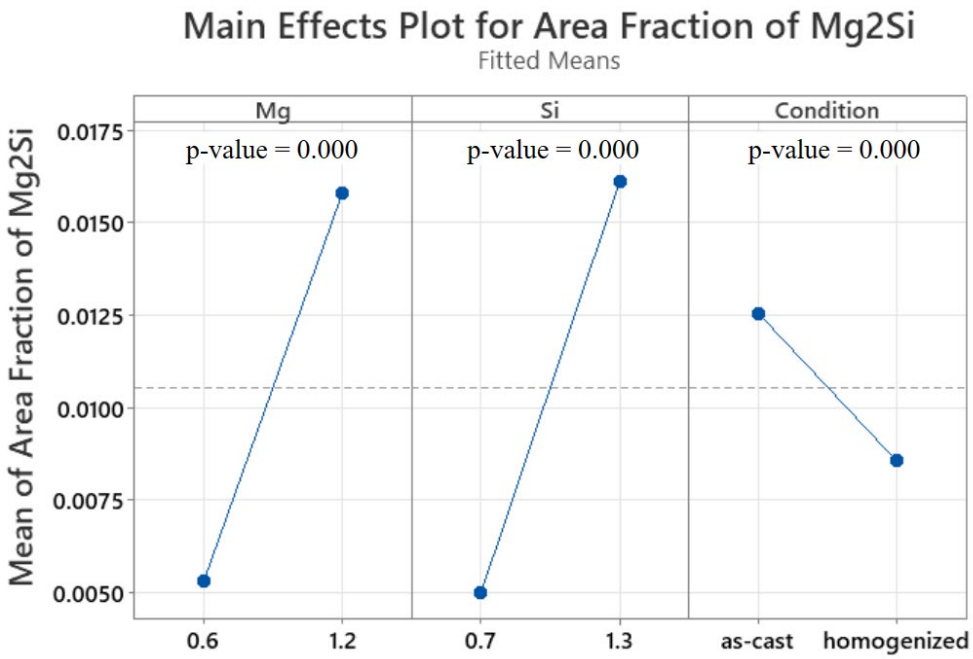

Figure 24. The main effects plot for the area fraction of Mg_2Si in the as cast and homogenized condition.

3.2.2 Average Particle Area Mg_2Si

Image analysis of the as cast and homogenized samples for the five DOE compositions was performed to assess the average particle area for Mg_2Si (Figure 25). Both Mg and Si increased the average size of Mg_2Si precipitates in the as cast and homogenized condition. However, increasing Mg concentration did have a more significant effect at increasing the average particle size of Mg_2Si. It was also found that after homogenization the average particle size generally decreases for the alloy compositions (Figure 26).

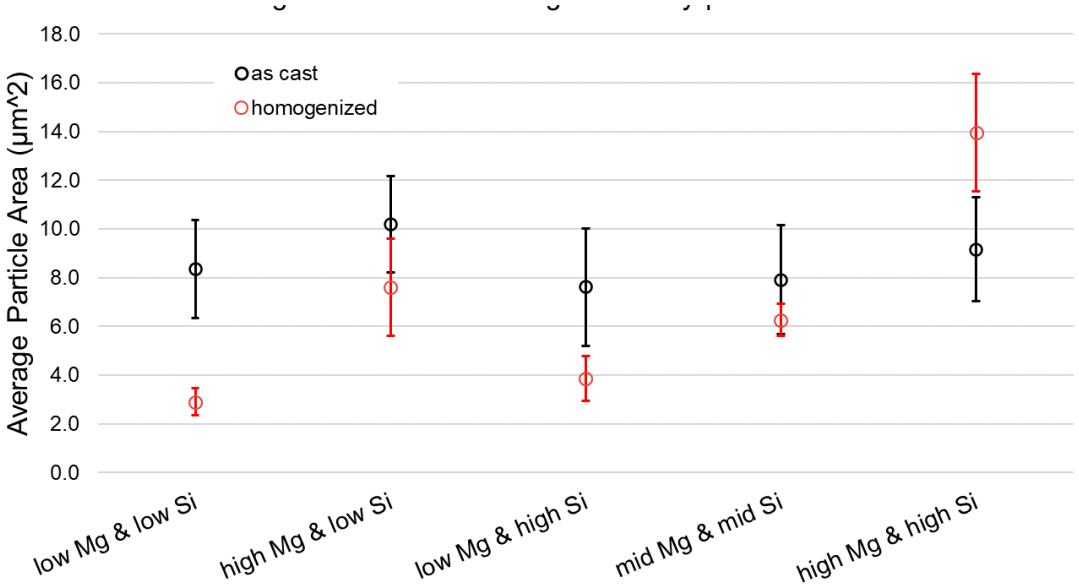

Figure 25. The average particle area for Mg_2Si per alloy type given the homogenized and as cast Condition. Note the error bars are 95% confidence in the standard error of the mean.

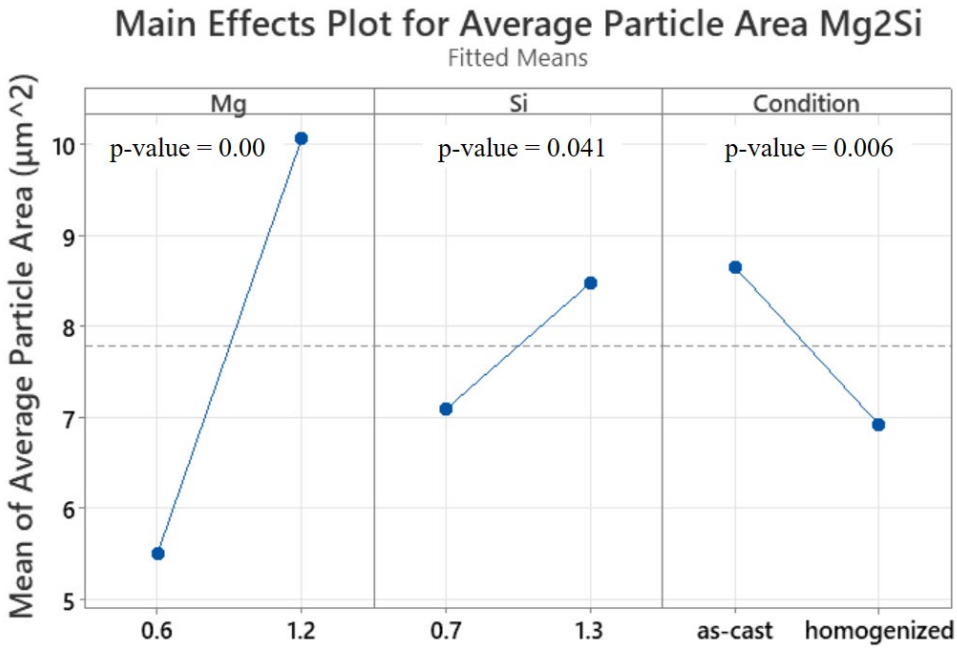

Figure 26. The main effects plot for the average particle area of Mg_2Si in the as cast and homogenized conditions.

3.2.3 Average Intermetallic Interdendritic Area Fraction

The average area fraction of the interdendritic region was analyzed to identify the effect of Mg, Si, and homogenization (Figure 27). There was a significant increase to the average area fraction of the intermetallic in the interdendritic region with increasing concentrations of Mg and Si in the 6082 alloys. There is also significant decrease in the intermetallic interdendritic area fraction after the homogenization heat treatment (Figure 28).

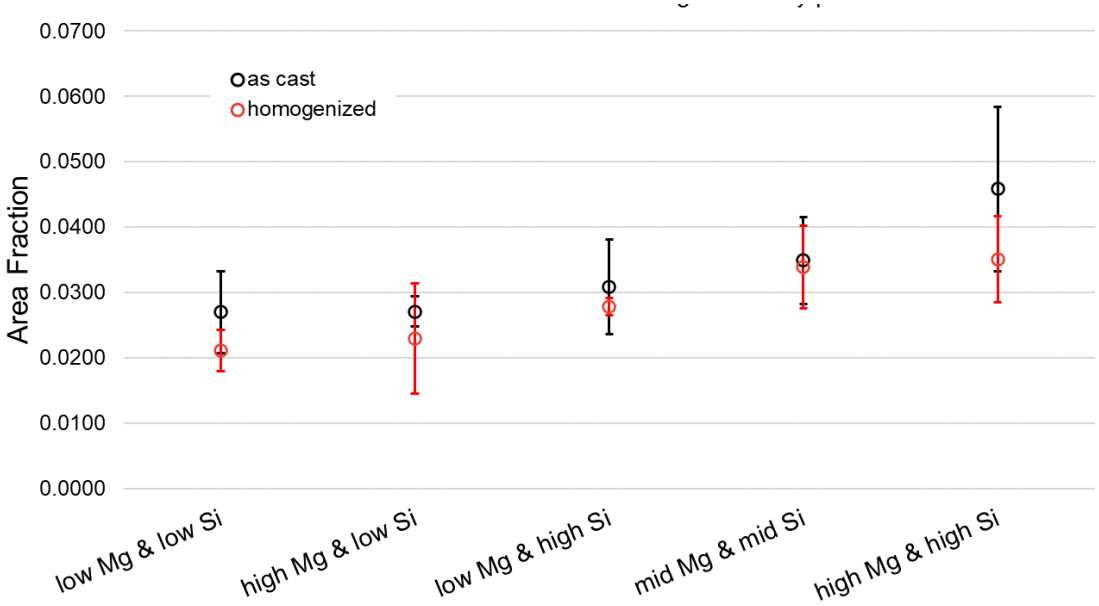

Figure 27. The area fraction of the intermetallic in the interdendritic region per alloy type in the as cast and homogenized condition. Note the error bars are 95% confidence in the standard error of the mean.

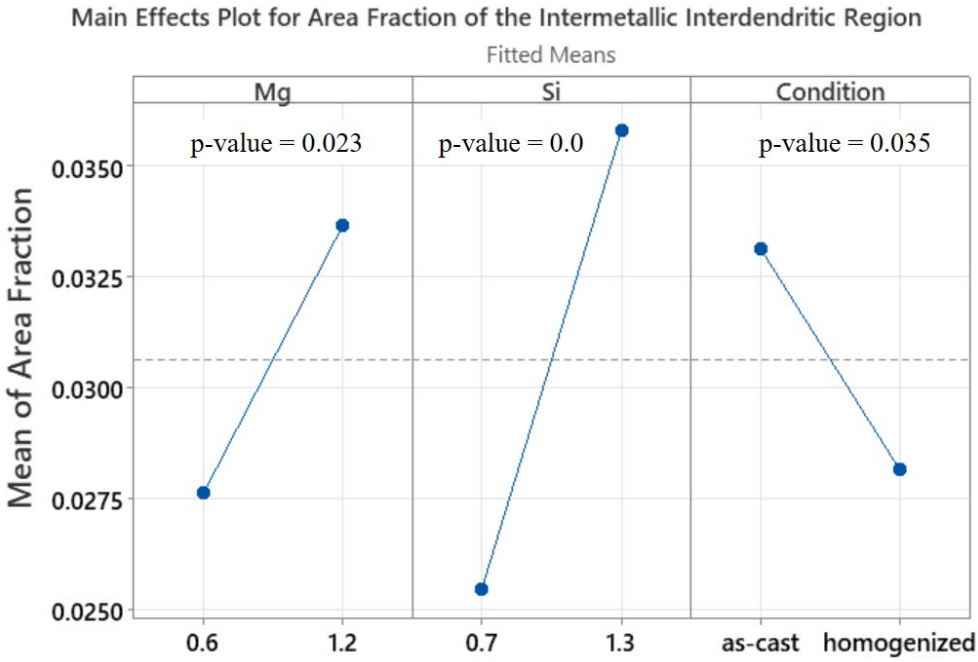

Figure 28. Main effects plot of the intermetallic area fraction of the intermetallic in the interdendritic region.

3.2.4 Average Particle Area of the Intermetallic Interdendritic Region

The average particle area for the intermetallic portion of the interdendritic region was analyzed to assess the differences between the five alloys, and the effect of the homogenization condition (Figure 29). It was found that there was no significant change in the average particle area given the changing Mg or Si concentration (Figure 30). However, there was a significant decrease in the particle area after the homogenization heat treatment.

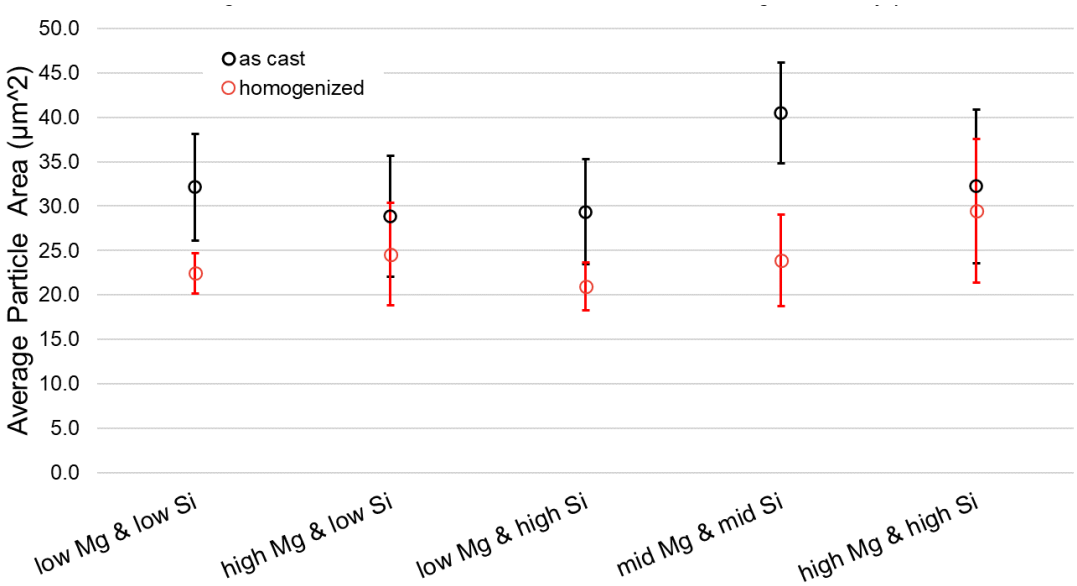

Figure 29. The average particle area of the intermetallic portion of the interdendritic region given the homogenized and as cast conditions. Note the error bars are 95% confidence in the standard error of the mean.

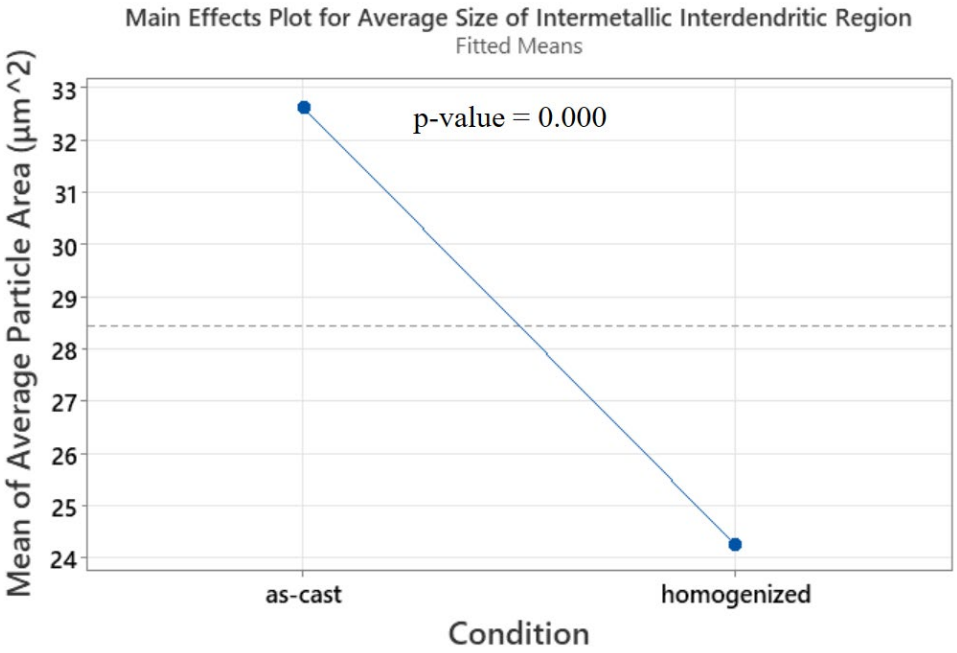

Figure 30. The main effects plot for the average particle area of the intermetallic in the interdendritic region. Note the rest of the factors were insignificant.

3.3 Hot Compression Testing Results

3.3.1 Flow Stress Results

Flow stress of the five 6082 alloys with varying Mg and Si concentration was tested with hot compression. The results of three conditions the high ln(Z) value of 400°C and a strain rate of 0.001 s^{-1} (Figure 31), the medium ln(Z) value of 450°C and a strain rate of 0.01 s^{-1} (Figure 33), and the low ln(Z) value of 500°C and a strain rate of 0.001 s^{-1} (Figure 35). The compression results for the high ln(Z) condition at 400°C and a strain rate of 0.1 s^{-1} showed that with statistical significance at a true strain of 0.1 increasing concentrations of Mg and Si increased the flow stress (Figure 32). The interaction results show the Si concentration had a synergistic impact on the flow stress when increasing the Mg concentration. For the medium ln(Z) condition at 450°C and a strain rate of 0.01 s^{-1} condition increasing Mg and increasing Si concentration increased the high temperature flow stress except the results are statistically insignificant (Figure 34). At the low ln(Z) condition of 500°C and a strain rate of 0.001 s^{-1}, increasing Mg concentration had a statistically insignificant decrease in the flow stress, while increasing Si had a statistically significant increase to the flow stress (Figure 36).

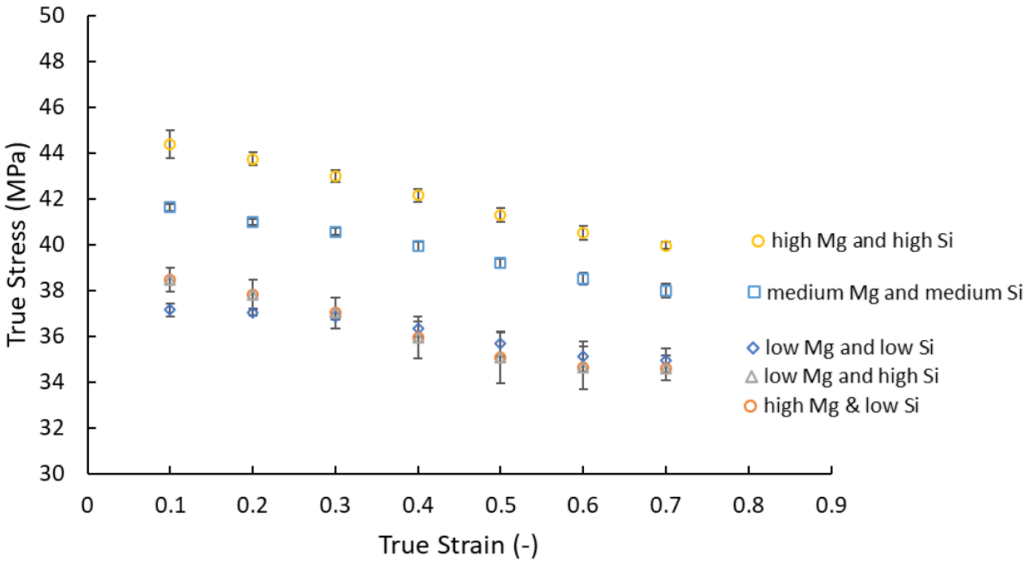

Figure 31. The average flow stress for the 400°C and a strain rate of 0.1 s^{-1} for the five alloys at selected values of true strain. Note the error bars are the 95% confidence intervals of the mean for the average of the three test runs.

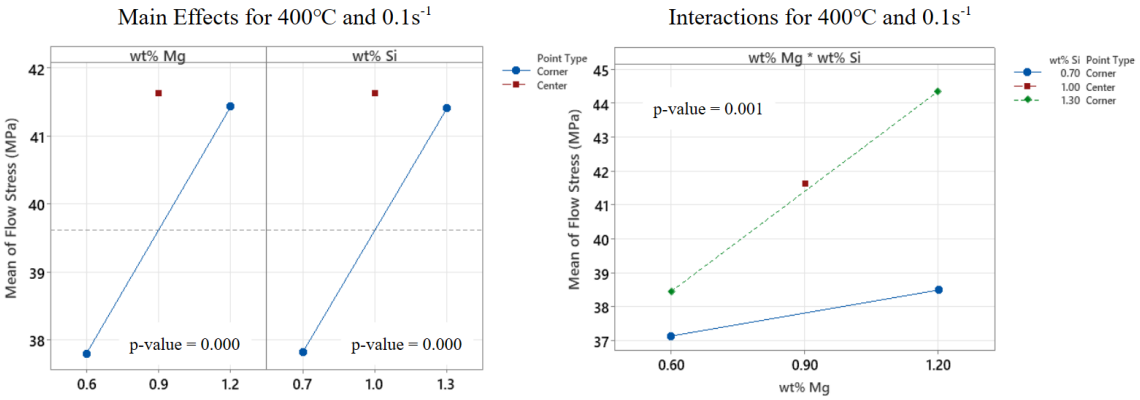

Figure 32. The main effects and interaction plot for the flow stress at 400°C and a strain rate of 0.1 s^{-1} for changing levels of Mg and Si.

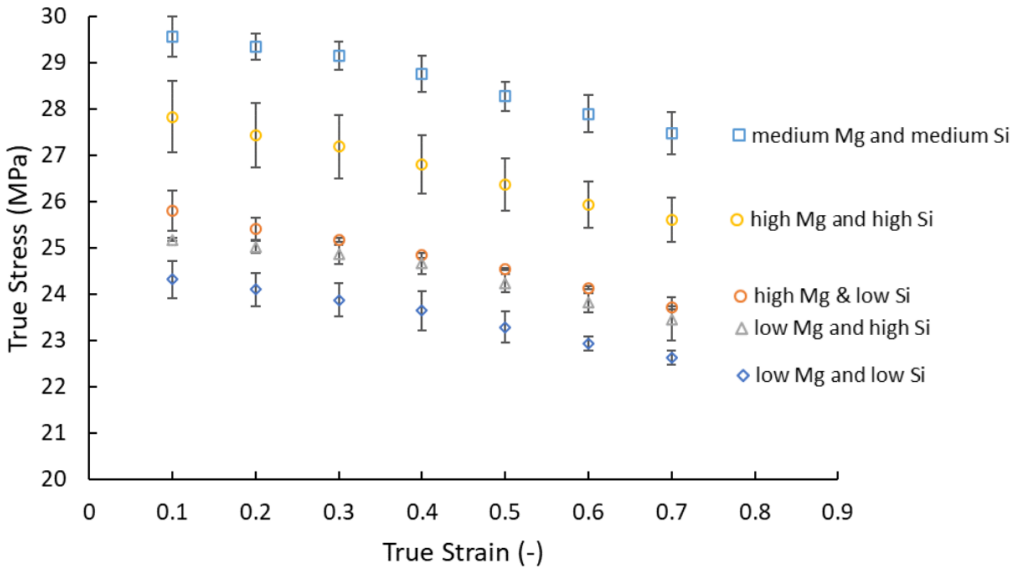

Figure 33. The average flow stress for the 450°C and a strain rate of 0.01 s^{-1} for the five alloys at selected values of true strain. Note the error bars are the 95% confidence intervals for the averages of the three test runs.

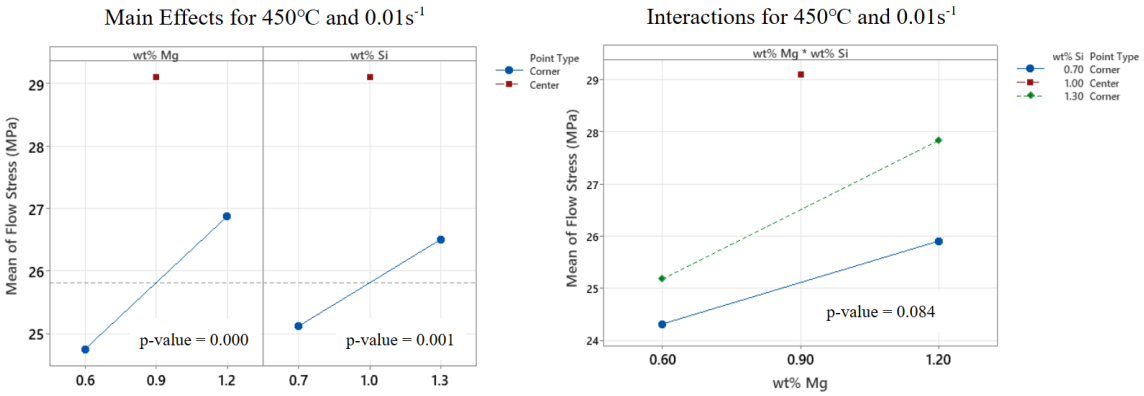

Figure 34. The main effects and interaction plot for the flow stress at a true stress of 0.1 for the condition 450°C and a strain rate of 0.01 s^{-1}.

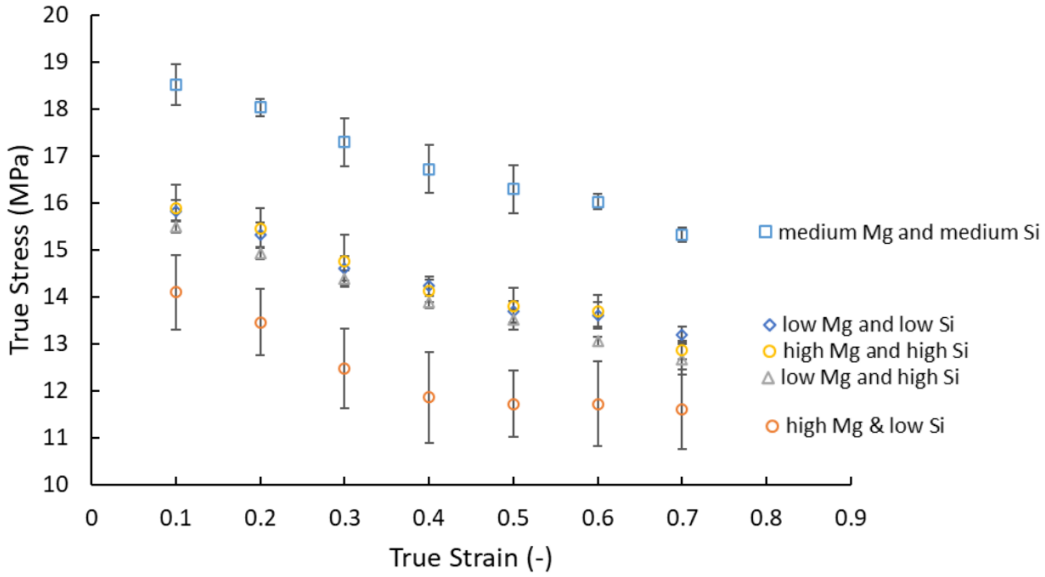

Figure 35. The average flow stress for the 500°C and a strain rate of 0.001 s^{-1} for the five alloys at selected values of true strain. Note the error bars are the 95% confidence intervals for the averages of the three test runs.

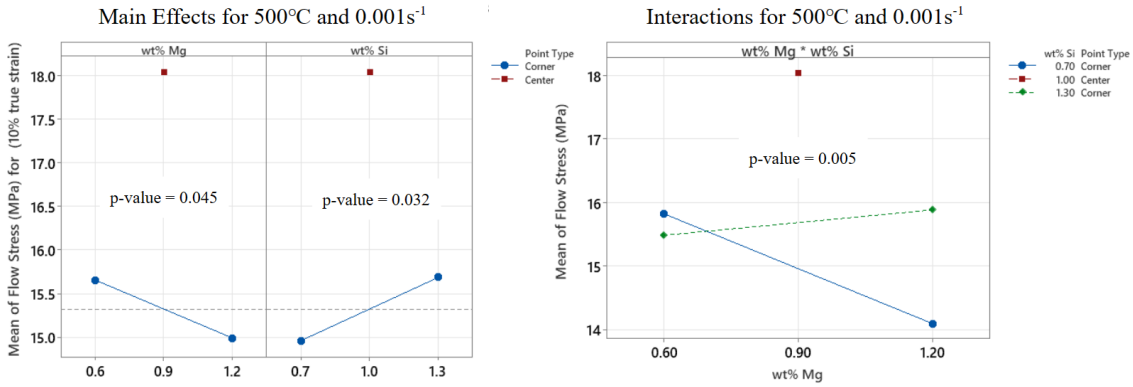

Figure 36. The main effects and interaction plot for the flow stress at a true stress of 0.1 for the condition 500°C and a strain rate of 0.001 s^{-1}.

3.3.2 Activation Energy for Hot Deformation

Inverse hyperbolic sine law is used for fitting flow stress curves for analysis of the activation energy for each alloy (Table 13). The raw data for the fitting analysis can be found in Appendix 3. (Figure 54 to 58). The highest value of activation energy is 292 ±

15 kJ/mol for the low Mg and high Si alloy and lowest value for activation energy is 220 ± 26 kJ/mol for the high Mg and low Si alloy. The main effects analysis of Mg and Si concentration on the activation energy showed that an increasing Mg content decreased the activation energy while increased Si increased the activation energy (Figure 37).

Table 13. The alpha value, stress exponent, activation energy, and reciprocal strain rate factor

Alloy	α (MPa^{-1})	n	Q ($kJ*mol^{-1}$)	ln[A] (s^{-1})
low Mg & low Si	0.036	9.0 ± 0.5	262 ± 15	45.1
high Mg & low Si	0.039	7.2 ± 0.9	220 ± 26	36.5
low Mg & high Si	0.041	9.6 ± 0.5	292 ± 15	48.9
medium Mg & medium Si	0.037	9.2 ± 0.6	248 ± 15	39.8
high Mg & high Si	0.038	7.7 ± 0.6	268 ± 20	44.5

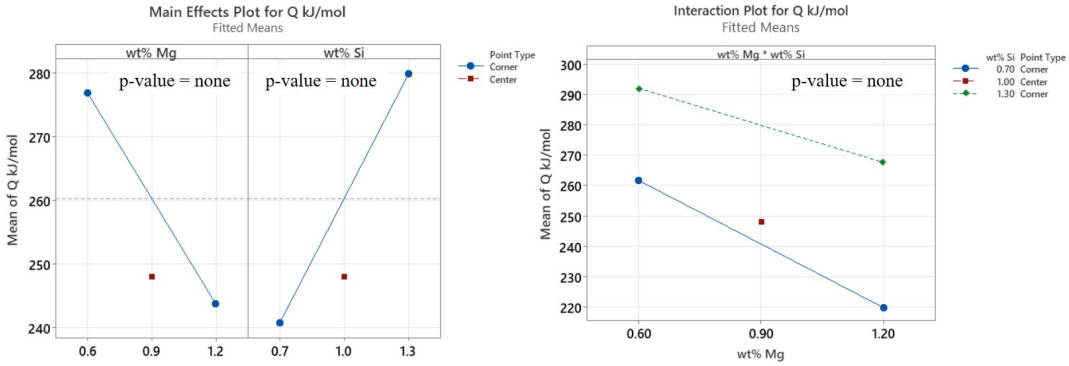

Figure 37. The main effects plot for the effect of Mg and Si concentration on the activation energy for hot deformation. Note due to the calculation method statistical analysis could not be performed.

3.4 EBSD Analysis

Electron backscattered diffraction analysis was performed on the five alloys and the fraction recrystallized was reported (Figure 38). Imaging was performed at the high ln(Z) value of 400°C and a strain rate of 0.1 s^{-1} (Figure 39), medium ln(Z) value of 450°C and a strain rate of 0.01 s^{-1} (Figure 40), and low ln(Z) value of 500°C and a strain rate of 0.001 s^{-1} (Figure 40). The highest fraction of recrystallization was identified to be 0.373

for the low Mg and low Si alloy at the low ln(Z) value. The lowest fraction of recrystallization identified to be 0.096 was identified for the low Mg and high Si alloy at the high ln(Z) value. The main effects of Mg and Si were also analyzed to determine their effect independent of the ln(Z) condition it was identified that increasing Mg did not have a significant effect on recrystallization while increasing Si did have a significant effect in decreasing the fraction of recrystallization (Figure 42). It was also found that the increases in Mg and Si did have significant interactions (Figure 43).

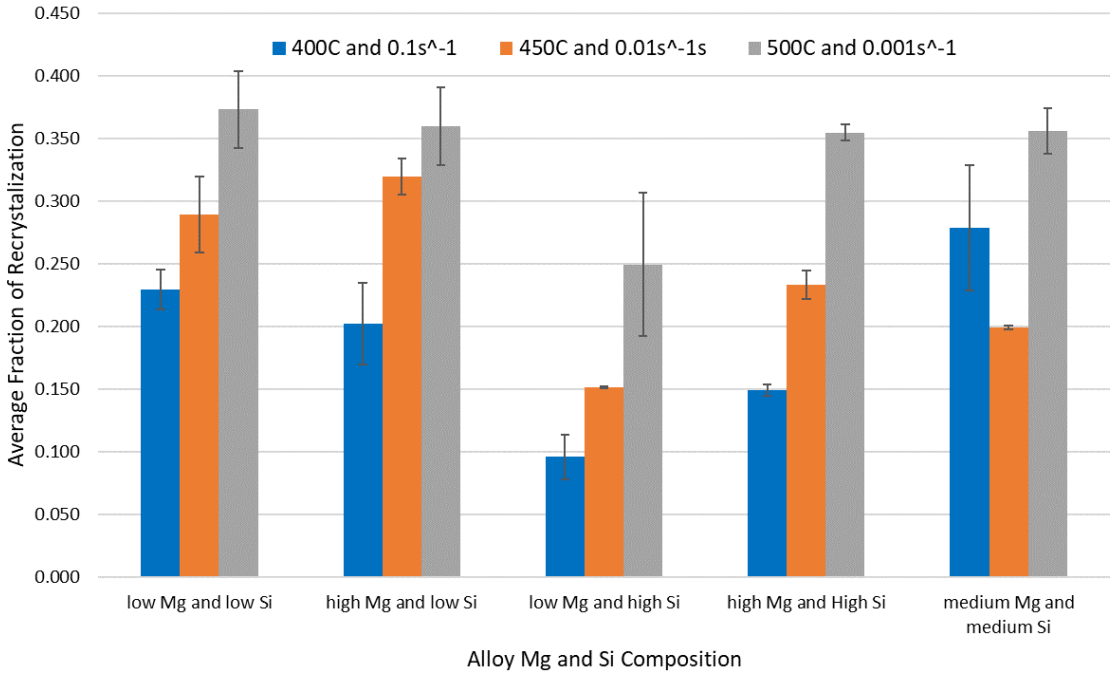

Figure 38. The average fraction of recrystallization of the five alloy compositions at the high ln(Z) (400°C and a strain rate of 0.1 s^{-1}), medium ln(Z) (450°C and a strain rate of 0.01 s^{-1}), and low ln(Z) (500°C and a strain rate of 0.001 s^{-1}) conditions. The error bars are 95% standard deviations of the mean.

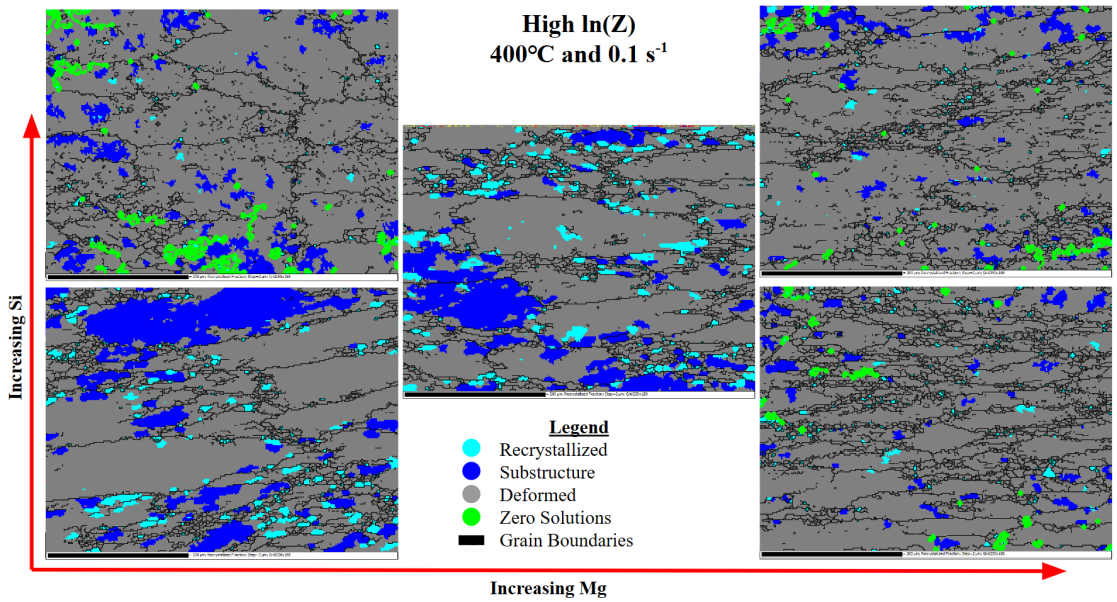

Figure 39. The microstructure of the as deformed compression samples for the five alloys at 400°C and a strain rate of 0.1 s^{-1} the high ln(Z) condition.

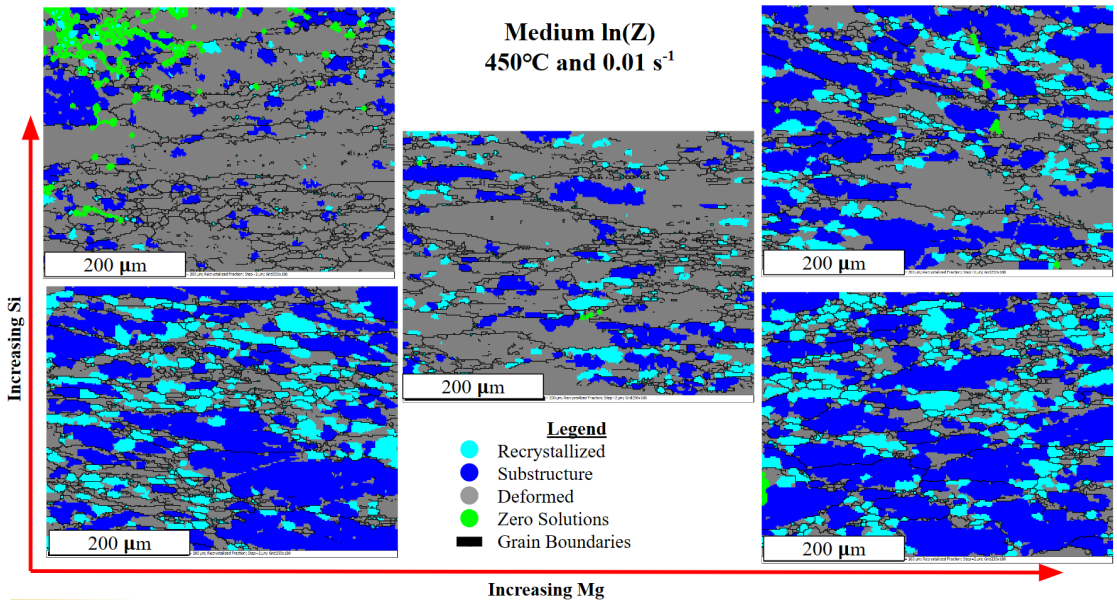

Figure 40. The microstructure of the as deformed compression samples for the five alloys at 450°C and a strain rate of 0.01 s^{-1} the medium ln(Z) condition.

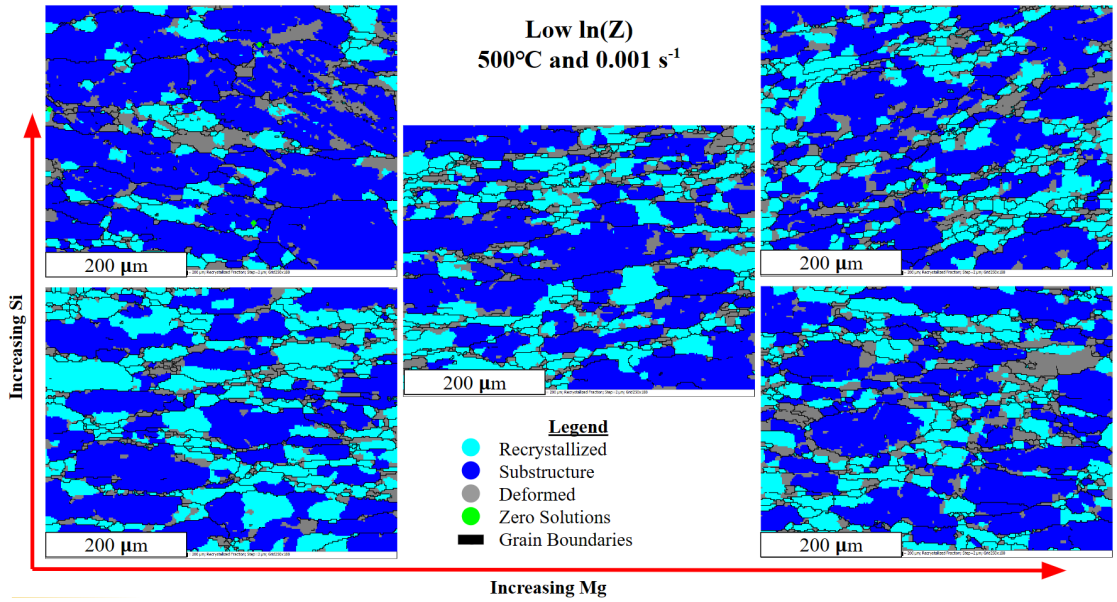

Figure 41. The microstructure of the as deformed compression samples for the five alloys at 500°C and 0 a strain rate of 0.001 s^{-1} the low ln(Z) condition.

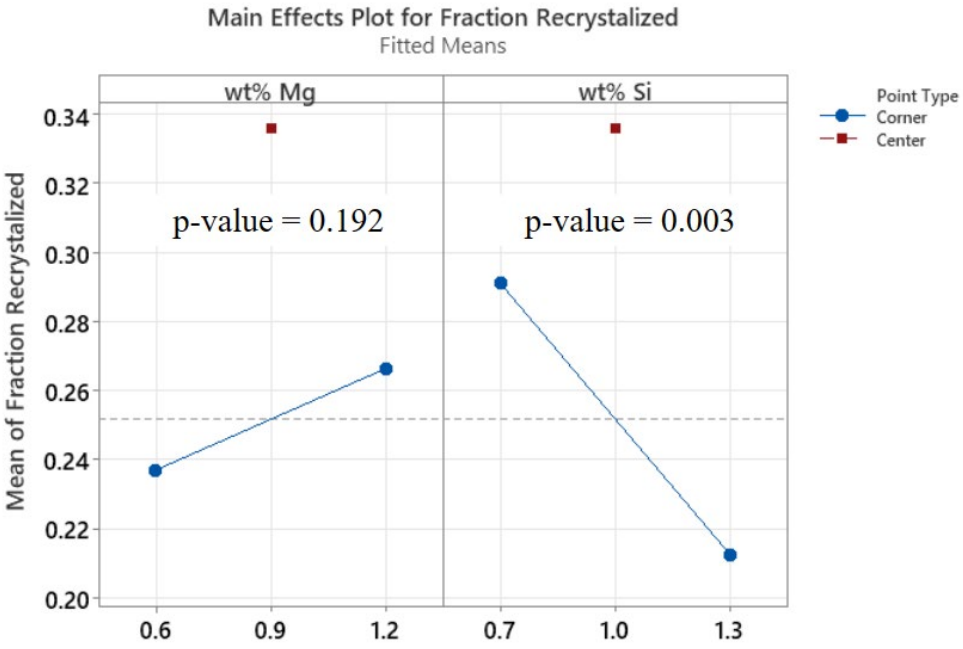

Figure 42. Main effects plot for the fraction of recrystallization after compression given the different Mg and Si levels for the high, medium, and low ln(Z) conditions.

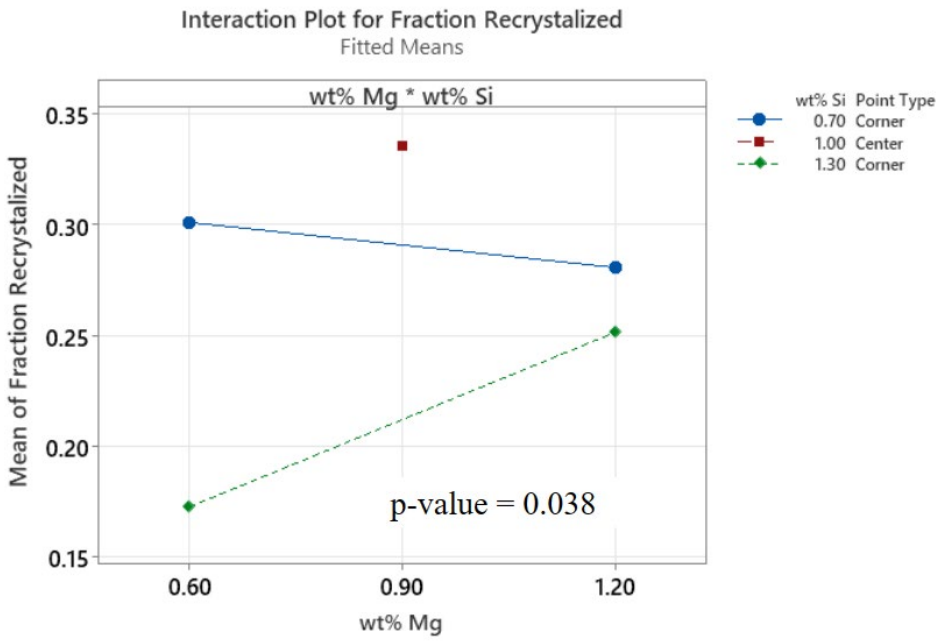

Figure 43. The interaction plot for wt% Mg and wt% Si on the mean fraction of recrystallization after compression testing.

4.0 Discussion

4.1 The Effect of Homogenization on the 6082 Compositions

Homogenization of the 6082 alloy is a critical component in the thermal history of the alloy as it can influence the flow stress and the dynamic recovery and recrystallization processes. The five alloys after homogenization showed significant reductions in the area fraction and particle size of Mg_2Si. However, some differences between the alloys may influence trends in the final hot deformation properties with the varying Mg and Si concentration. The high Mg and high Si alloy showed a significantly higher area fraction and particle size for Mg_2Si than the other four alloys, having an Mg_2Si particle size of 14 μm^2 and a total area fraction of 0.021 (Figure 44). The Mg_2Si in the high Mg and high Si alloy has an average particle size of 6 um^2 and a fraction of 0.011 Mg_2Si greater than the other alloys. Research has shown an increasing concentration of Mg_2Si caused by slower cooling rates leads to a significant reduction in the flow stress [24]. These changes in particle size and concentration will correspond to a decrease in the flow stress and activation energy results.

The homogenization heat treatment significantly affected the interdendritic intermetallic area fraction and particle size. After homogenization, all alloys' interdendritic portion of the intermetallic region decreased in area fraction and particle size. However, when increasing Si from 0.7 wt% to 1.3 wt%, the intermetallic area fraction increased from 0.020 to 0.028. No significant changes were identified for the average particle size, given the increase in Si. The increase in the intermetallic region is associated with an increasing dispersoid count [26]. Therefore, it can be assumed that

alloys with higher concentrations of Si will have higher fractions of dispersoids in the microstructure influencing the recrystallization properties.

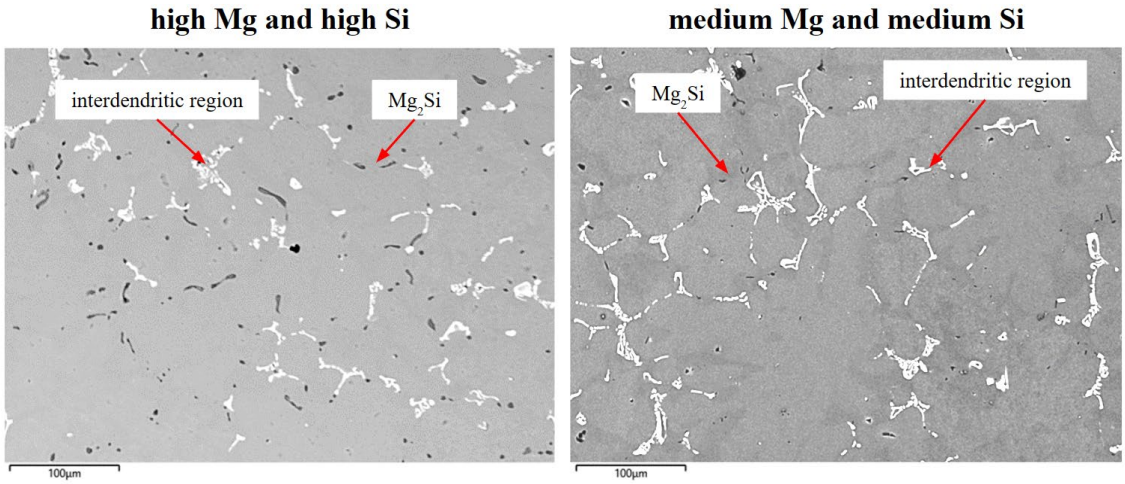

Figure 44. Comparison of the microstructure of the high Mg and high Si alloy vs. the medium Mg and medium Si alloy in the homogenized condition showing the dark phase, which is Mg_2Si, and light phase containing Cr, Fe, Si, and Mn, which is in the interdendritic region.

4.2 The Effect of Mg and Si on the High-Temperature Flow Stress of the 6082 Aluminum

The composition of the 6082 alloy is modified with Mg and Si to determine the effect of the elements on the high-temperature flow stress and hot deformation activation energy. As noted with the homogenization results, increasing Mg and Si concentration had an associated increase in the particle size and area fraction of both the Mg_2Si phase and the intermetallic after the homogenization heat treatment. Despite these effects, there are trends in the flow stress, which can be described by increasing concentrations of Mg and Si. For the high ln(Z) and medium ln(Z) conditions, increasing Mg from 0.6 to 1.2 wt% and Si from 0.7 to 1.3 wt% led to increased high-temperature flow stress. The

changes in flow stress can be attributed to the increases in the amount of precipitates and dispersoids caused by increasing concentrations of Mg and Si. The high Mg and high Si alloy had the highest flow stress for the high ln(Z) condition, while the medium Mg and medium Si alloy had the highest flow stress for the medium ln(Z) and low ln(Z) values. The increased flow stress of the medium Mg and medium Si alloys is due to the smaller particle size and area fraction of Mg_2Si between the two alloys (Figure 45). The larger size of the Mg_2Si precipitates increased flow stress at lower temperatures and faster strain rates but decreased flow stress with increasing temperature and slower strain rates. This effect is caused by a switch in the deformation mechanism, which favors more dynamic recrystallization instead of dynamic recovery. The difference in recrystallization between the two alloys can be seen in the medium ln(Z) condition, where the high composition has a higher fraction of recrystallization than the medium composition (Figure 38). The increased fraction of recrystallization is caused by the larger fraction and size of Mg_2Si precipitates, which act as nucleation sites for new grain formation, increasing the amount of recrystallization [34]. The recrystallization properties were, however, not significantly affected by the Mg and Si concentration at the high ln(Z) condition for the two compositions, although there was a decrease in the flow stress between the two alloys at the high ln(z) condition.

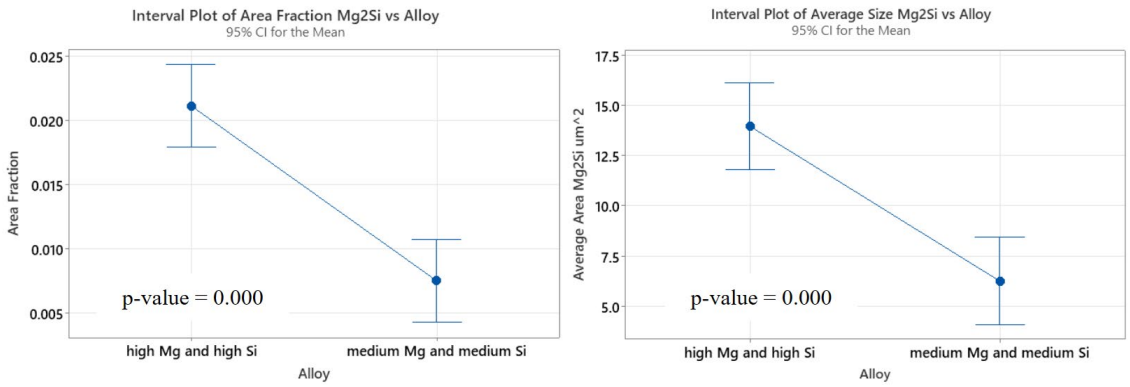

Figure 45. One-way ANOVA analysis of the average size and area fraction of Mg_2Si between the high Mg and high Si alloy and the medium Mg and medium Si alloy.

Another trend observed in the flow stress regarding the low ln(Z) condition was the increase in flow stress with an increase in Si from 0.7 to 1.3 wt% at a constant Mg concentration of 0.6 wt%. The high Si and low Mg alloy had a large fraction of intermetallic, indicating that more dispersoids are present (Figure 46). The increase in dispersoid content improved recrystallization resistance by pinning grain boundaries during hot deformation. This behavior is proven by the recrystallization results, which showed that the low Mg and high Si alloy had the lowest fraction of recrystallization for all alloys at every ln(Z) condition. This higher recrystallization resistance made hot deformation more difficult therefore increasing the flow stress of the high Si alloy.

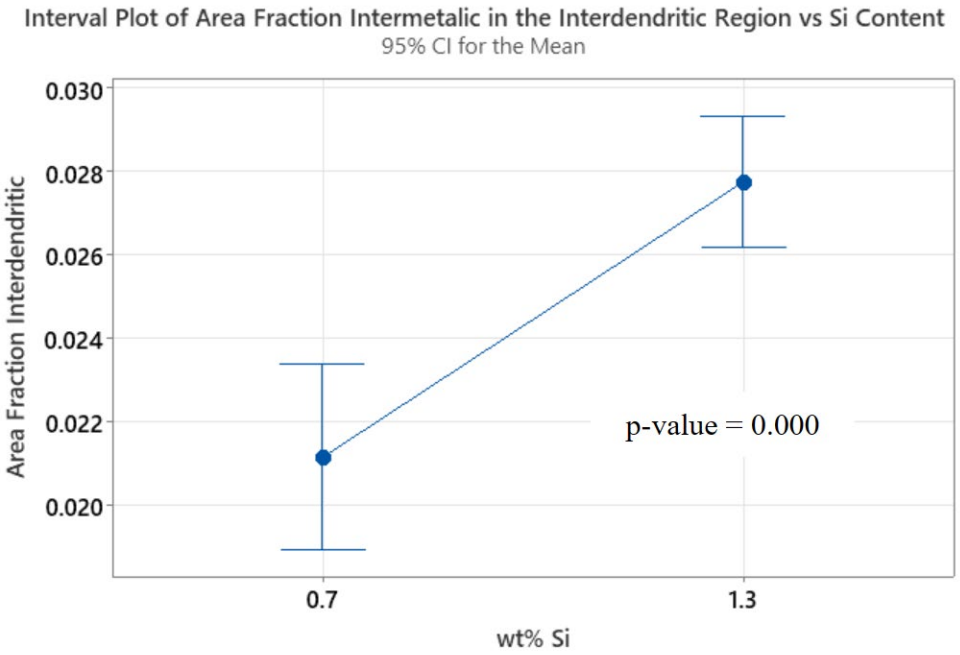

Figure 46. One-way ANOVA analysis for the area fraction interdendritic intermetallic v. the concentration of Si at constant Mg concentration.

4.3 The Effect of Mg and Si on the Hot Deformation Activation Energy

The concentration of Mg and Si independently had significant effects on the activation energy when compared to the low composition of 0.6 wt% Mg and 0.7 wt% Si. When the Mg concentration increases from 0.6 to 1.2 wt% with constant Si of 0.7 wt%, the activation energy decreases from 262 to 220 kJ/mol. However, when the Si concentration increases from 0.7 to 1.3 wt% with a constant concentration of 0.6 wt% Mg, the activation energy increases from 262 to 292 kJ/mol. The increase in Mg concentration had a greater effect on the activation energy than Si, changing the average activation energy by 10 kJ/mol more. This change in activation energy shows that the dispersoid concentration affects the activation energy less than the Mg additions. The

changes to the activation energy are also related to the recrystallization results, which show that for each ln(Z) condition, the high Mg and low Si alloys had greater fractions of recrystallization compared to the low Mg high Si alloy.

Despite the effects of the individual concentration of Mg and Si on the activation energy, it was found that there is minimal change when the composition of Mg and Si equally increases in wt%. For example, when the concentration of Mg and Si were both increased by 0.3 wt% to the center point composition, the activation energy decreased from 262 to 248 kJ/mol. When the composition was further increased by another 0.3 wt%, the activation increased from 248 to 268 kJ/mol. These changes in activation energy between the three compositions were found to be statistically insignificant. There were, however, some variations between these three compositions and the alloys, which had only independently changing Si and Mg concentrations. When increasing the Mg with constant Si, the activation energy decreases more than in alloys with constant ratio compositions. The activation energy then increases when increasing the Si with a constant Mg concentration. These relations show that having excess Si increases the activation while having excess Mg will decrease the activation energy compared to a composition with a Mg to Si ratio near 0.9. It also suggests that increasing dispersoids density positively affects the activation energy while increasing solid solution negatively affects the activation energy.

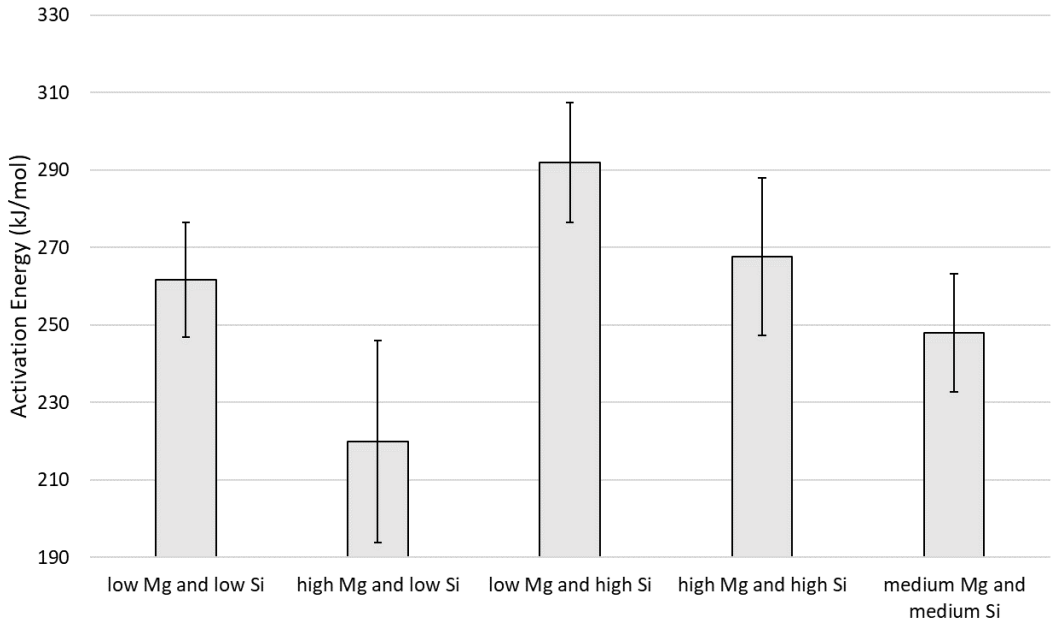

Figure 47. Comparison of the activation energies for the five alloys tested. The error bars are propagated error from the hyperbolic sine fitting method.

4.4 The Effect of Mg and Si on the Dynamic Recovery and Recrystallization of the 6082 Aluminum

The recrystallization response of the different alloys was related to the changing concentrations of Mg and Si. The combined effects of increasing both Mg and Si to the medium and high concentrations had an insignificant effect on the recrystallization properties for the low and high ln(Z) conditions. However, the medium Mg and medium Si alloy did significantly decrease the recrystallization fraction at the medium ln(Z) condition when compared to the low and high alloys.

An effect is also observed as only the Mg concentration increases while the Si level stays constant. The average recrystallized fraction increased but had an insignificant effect even though the alloy had an observed decrease in activation energy and flow stress at the high ln(Z) condition when compared to the low Mg and low Si alloy. These

responses indicate more recrystallization, which has been linked with decreasing activation energy and flow stress at high temperatures.

The effect of only increasing Si was also analyzed. It was found that as the concentration of Si increased, the fraction of recrystallization decreased. As the high concentration of Si was found to primarily increase the amount of the interdendritic intermetallic, the increase in intermetallic is believed to be associated with an increase in dispersoid concentration which is primarily made of Cr, Fe, Mn, and Si. An increase in dispersoid concentration will decrease the fraction of recrystallization due to Zener pinning, which slows grain boundary motion and aids in resisting the recrystallization process. This behavior is linked to the increased activation energy, which has also been shown to increase with dispersoid density [18].

4.5 Hypothesis

- If the Mg concentration in 6082 is increased to the high specification limit, then the fraction of low-angle grain boundaries will decrease because the increase in Mg solute will inhibit dynamic recovery and favor recrystallization.

The increase in Mg concentration **did not** lead to a significant increase in the fraction of recrystallization for the medium and low ln(Z) values. However, the high Mg and low Si composition was found to have the lowest activation energy for hot deformation compared to all other alloys. The high Mg and low Si alloy was also identified to have the lowest flow stress at the low ln(Z) value. As the low ln(Z) value is the best condition for recrystallization and has low activation energies associated with improved recrystallization, it is suspected that the increased Mg composition did recrystallize more even though it could not be measured using EBSD analysis.

- If the Si concentration in 6082 is increased to the high specification limit, then the fraction of low-angle grain boundaries will increase because the increase in Si-containing dispersoids will inhibit dynamic recrystallization and favor dynamic recovery.

The increase in Si concentration **did** decrease the amount of recrystallization in the 6082 alloy. It was found that the Si additions significantly reduced the amount of high-angle grain boundaries. The reduction was caused by increasing amounts of Si-containing dispersoids indicated by the larger area fractions of the interdendritic intermetallic, which contains the additions of Cr, Fe, Si, and Mn. The dispersoids increase the resistance to recrystallization through Zener pinning, which does not allow flow stress to decrease through recrystallization. The high Si alloy also had the highest activation energy of all other alloys, which is linked with reduced fractions of recrystallization.

- If the Mg and Si concentration is increased in a 6082 alloy, then the activation energy for hot deformation will increase because increases in solid solution decrease the stacking fault energy and therefore increase the energy required for dislocation motion.

The increase in both Mg and Si **did not** have a significant increase in the activation energy for hot deformation, but independently, the inclusion of Mg decreased the activation energy while the increase in Si increased the activation energy. These results showed that having excess Mg will lower activation energy and increase recrystallization, while excess Si will increase the activation energy and decrease recrystallization. Therefore, simultaneously increasing Mg and Si concentrations had a balancing effect that insignificantly altered the activation energy.

5.0 Conclusion

To better understand the effect of Mg and Si in 6082, these concentrations were modified at constant Cr, Fe, and Mn with the same homogenization heat treatment. It was identified that increasing Mg from 0.6 to 1.2wt% decreases the activation energy from 262 to 220 kJ/mol, while increases in Si from 0.7 to 1.3wt% decreases the recrystallization fraction and increases activation energy from 262 to 292 kJ/mol. However, for the high composition of 1.2 wt% Mg and 1.3 wt% Si, the amount of recrystallization and activation energy did not significantly change (Figure 48). The insignificant change in activation energy was caused by the increased fraction and particle size of Mg_2Si, which precipitated during the homogenization heat treatment. The 0.9 wt% Mg and 1.0 wt% Si alloy did not have a significant decrease in activation energy when compared to the 0.6 wt% Mg and 0.7 wt% Si composition. The composition did have a lower fraction of recrystallization at the medium ln(Z) value compared to both the low and high compositions for Mg and Si. However, there were insignificant differences between the high and low ln(Z) conditions, so the differences at the medium ln(Z) condition are believed to be significant. Therefore, the low, medium, and high compositions which have Mg to Si ratios of 0.95, 0.83, and 0.99 respectively are considered to have insignificant changes in activation energy and recrystallization.

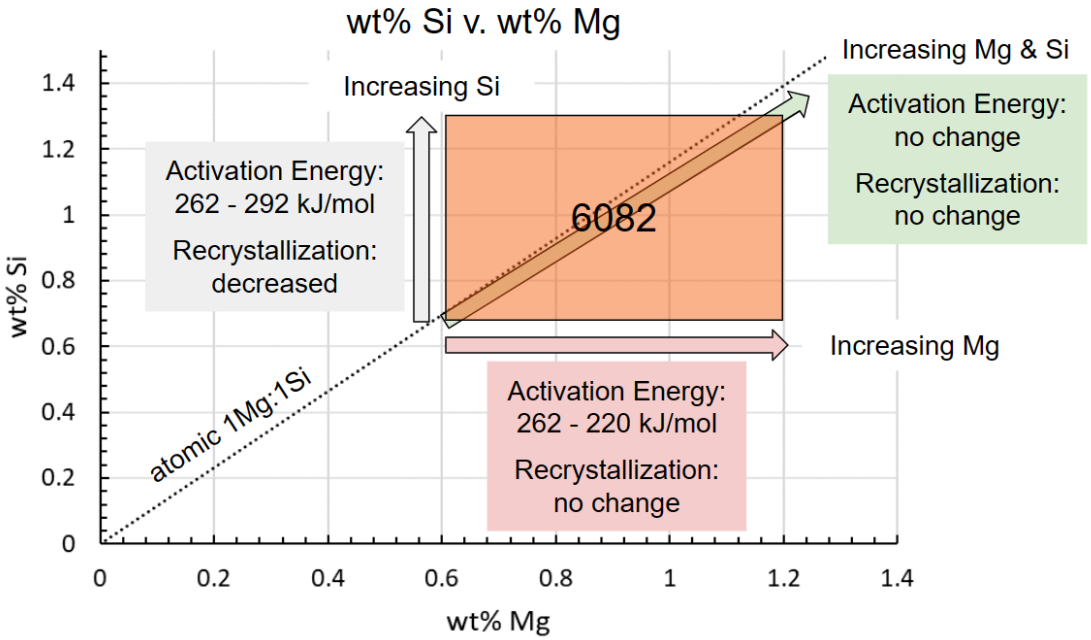

Figure 48. The wt% Si v. wt% Mg composition for the 6082 alloy highlighting the increasing Mg, increasing Si, and increasing both Mg and Si simultaneously.

Considering the effects of the hot deformation activation energy and the recrystallization after deformation, the 6082 alloy can be optimized to improve extrusion performance. As the ideal extrusion properties have a low fraction of recrystallization, activation energy, and flow stress, alloys which have ratio of Mg to Si which is between 0.8 and 1 did perform optimally given the selected homogenization condition and constituent alloying elements. To further optimize these alloys, consideration should be given to the homogenization as the fraction of intermetallic dispersoids and Mg_2Si precipitates is dependent on it, and these values had significant effects on the fraction of recrystallization, activation energy, and flow stress.

6.0 Reference List

[1] A. Schiffl, I. Schiffl, M. Hartmann, S. Brötz, J. Österreicher, and W. Kühlein, "Analysis of Impact Factors on Crash Performance of High Strength 6082 Alloys Consider Extrudability and Small Modifications of the Profile Geometry," *Mater. Today Proc.*, vol. 10, pp. 193–200, 2019, doi: 10.1016/j.matpr.2018.10.396.

[2] A. Schiffl, I. Schiffl, and J. Österreicher, "Identification of the Most Influencing Parameter for Perfect Extrudability of High-Strength 6082," *Elev. Int. Alum. Extrus. Technol. Semin. Expo.*, 2016.

[3] N. Hashimoto, "Application of Aluminum Extrusions to Automotive Parts," 2017.

[4] D. O. Odoh, "Effect of Alloy Composition on the Hot Deformation Behavior, Extrudability and Mechanical Properties of AA6XXX Aluminum Alloys," 2017.

[5] A. Poznak, "THE INFLUENCE OF PRIOR NATURAL AGING ON ARTIFICIAL AGE HARDENING IN AL-MG-SI ALLOYS," Doctor of Philosophy in Materials Science and Engineering, Michigan Technological University, Houghton, Michigan, 2017. doi: 10.37099/mtu.dc.etdr/455.

[6] P. K. Saha, *Aluminum Extrusion Technology*. ASM International, 2000. doi: 10.31399/asm.tb.aet.9781627083362.

[7] T. Sheppard, *Extrusion of Aluminum Alloys*, vol. 1. Springer Science & Business Media, 1999.

[8] L. Lodgaard and N. Ryum, "Precipitation of dispersoids containing Mn and/or Cr in Al–Mg–Si alloys," *Mater. Sci. Eng. A*, vol. 283, no. 1–2, pp. 144–152, May 2000, doi: 10.1016/S0921-5093(00)00734-6.

[9] C. L. Liu, Q. Du, N. C. Parson, and W. J. Poole, "The interaction between Mn and Fe on the precipitation of Mn/Fe dispersoids in Al-Mg-Si-Mn-Fe alloys," *Scr. Mater.*, vol. 152, pp. 59–63, Jul. 2018, doi: 10.1016/j.scriptamat.2018.04.012.

[10] B07 Committee, "Specification for Aluminum and Aluminum-Alloy Extruded Bars, Rods, Wire, Profiles, and Tubes," ASTM International. Accessed: May 15, 2023. [Online]. Available: http://www.astm.org/cgi-bin/resolver.cgi?B221-21

[11] M. N. Amado and F. Daroqui, "Revision of The Solvus Limit of Al-Mg2Si Pseudo Binary Phase Diagram," *Procedia Mater. Sci.*, vol. 8, pp. 1079–1088, 2015, doi: 10.1016/j.mspro.2015.04.171.

[12] N. Lu, J. Wang, and C.-H. Zhang, “First-principles study of the structural and mechanical properties of substitution-doped Mg5Si6,” *J. Mater. Res.*, vol. 37, no. 18, pp. 2996–3008, Sep. 2022, doi: 10.1557/s43578-022-00703-1.

[13] E. Fahri Ozdogru, “The Effect of Chemical Composition on EN AW 6XXX Series Aluminum Alloys,” in *Recent Advancements in Aluminum Alloys [Working Title]*, IntechOpen, 2023. Accessed: Jun. 06, 2023. [Online]. Available: https://www.intechopen.com/online-first/86386

[14] C. Liu, “MICROSTRUCTURE EVOLUTION DURING HOMOGENIZATION AND ITS EFFECT ON THE HIGH TEMPERATURE DEFORMATION BEHAVIOUR IN AA6082 BASED ALLOYS,” 2008.

[15] N.C. Parson, “The Effect of Heat Treatment on the Microstructure and Properties of 6xxx Series Alloy Extrusion Ingots,” *Miner. Met. Mater. Soc.*, no. Light Metals, 1989.

[16] M. Kenyon, J. Robson, J. Fellowes, and Z. Liang, “Effect of Dispersoids on the Microstructure Evolution in Al – Mg – Si Alloys,” *Adv. Eng. Mater.*, vol. 21, no. 4, p. 1800494, Apr. 2019, doi: 10.1002/adem.201800494.

[17] B. Treanore, “ANALYZING VARIATION IN DISPERSOID FORMATION IN ALUMINUM ALLOYS BY MINOR CHANGES IN HOMOGENIZATION TEMPERATURE,” Master of Science in Materials Science and Engineering, Michigan Technological University, Houghton, Michigan, 2021. Accessed: May 12, 2023. [Online]. Available: https://digitalcommons.mtu.edu/etdr/1349

[18] X. Wang, J. Qin, H. Nagaumi, R. Wu, and Q. Li, “The Effect of α -Al(MnCr)Si Dispersoids on Activation Energy and Workability of Al-Mg-Si-Cu Alloys during Hot Deformation,” *Adv. Mater. Sci. Eng.*, vol. 2020, pp. 1–12, May 2020, doi: 10.1155/2020/3471410.

[19] H. Lin, “Dynamic recrystallization behavior of 6082 aluminum alloy during hot deformation,” *Adv. Mech. Eng.*, vol. 13, no. 9, p. 168781402110461, Sep. 2021, doi: 10.1177/16878140211046107.

[20] S. Tomovic-Petrovic and O. Jensrud, “Extrusion of silicon-rich AlMgSi alloys,” *J. Mater. Process. Technol.*, vol. 212, no. 6, pp. 1437–1442, Jun. 2012, doi: 10.1016/j.jmatprotec.2012.02.004.

[21] M. S. Remøe, K. Marthinsen, I. Westermann, K. Pedersen, J. Røyset, and C. Marioara, “The effect of alloying elements on the ductility of Al-Mg-Si alloys,” *Mater. Sci. Eng. A*, vol. 693, pp. 60–72, May 2017, doi: 10.1016/j.msea.2017.03.078.

[22] F. J. Humphreys and M. Hatherly, *Recrystallization and related annealing phenomena*, 1st ed. Oxford, OX, UK ; Tarrytown, N.Y., U.S.A: Pergamon, 1995.

[23] Q. Guo-Zheng, "Characterization for Dynamic Recrystallization Kinetics Based on Stress-Strain Curves," in *Recent Developments in the Study of Recrystallization*, P. Wilson, Ed., InTech, 2013. doi: 10.5772/54285.

[24] M. A. Mostafaei and M. Kazeminezhad, "A novel approach to find the kinetics of dynamic recovery based on hot flow curves," *Mater. Sci. Eng. A*, vol. 544, pp. 88–91, May 2012, doi: 10.1016/j.msea.2012.02.093.

[25] W. Ding *et al.*, "Hot Deformation Behavior and Microstructure Evolution of 6063 Aluminum Alloy Modified by Rare Earth Y and Al-Ti-B Master Alloy," *Materials*, vol. 13, no. 19, p. 4244, Sep. 2020, doi: 10.3390/ma13194244.

[26] T. Sheppard, "Temperature and speed effects in hot extrusion of aluminium alloys," *Met. Technol.*, vol. 8, no. 1, pp. 130–141, Jan. 1981, doi: 10.1179/030716981803276009.

[27] S. Zajac, B. Bengtsson, A. Johansson, and L.-O. Gullman, "Optimisation of Mg_2Si Phase for Extrudability of AA 6063 and AA 6005 Alloys," *Mater. Sci. Forum*, vol. 217–222, pp. 397–402, May 1996, doi: 10.4028/www.scientific.net/MSF.217-222.397.

[28] X. Qian, N. Parson, and X.-G. Chen, "Effects of Mn addition and related Mn-containing dispersoids on the hot deformation behavior of 6082 aluminum alloys," *Mater. Sci. Eng. A*, vol. 764, p. 138253, Sep. 2019, doi: 10.1016/j.msea.2019.138253.

[29] R. F. Wall, "Extrusion of Alumium Alloys," *J. Air Transp. Div.*, vol. 85, no. 3, pp. 57–62, Jul. 1959, doi: 10.1061/JACEAL.0000070.

[30] O. Reiso, "Extrusion of AlMgSi Alloys," *Proc. 9th Int. Conf. Alum. Alloys*, 2004.

[31] D. Hull and D. J. Bacon, *Introduction to dislocations*, 5. ed. Amsterdam Heidelberg: Butterworth Heinemann, Elsevier, 2011.

[32] Ø. Ryen, B. Holmedal, O. Nijs, E. Nes, E. Sjölander, and H.-E. Ekström, "Strengthening mechanisms in solid solution aluminum alloys," *Metall. Mater. Trans. A*, vol. 37, no. 6, pp. 1999–2006, Jun. 2006, doi: 10.1007/s11661-006-0142-7.

[33] H. Jazaeri and F. J. Humphreys, "Quantifying recrystallization by electron backscatter diffraction: QUANTIFYING RECRYSTALLIZATION BY EBD," *J. Microsc.*, vol. 213, no. 3, pp. 241–246, Feb. 2004, doi: 10.1111/j.0022-2720.2004.01296.x.

[34] F. J. Humphreys and M. Hatherly, *Recrystalization and Related Annealing Phenomena: Second Edition*. Elsevier, 2004.

A.0 Appendix

A.1 Equations Used for Compression Testing Analysis

Compression testing analysis is performed with the use of MATLAB given data exported from the MTS test suite software. The true stress is calculated using (Equation 5) where F is the instantaneous load, h_o is the original height, D_o is the original diameter, and Δh is the change in height and true strain is calculated using (Equation 6). A correction factor is applied to the uncorrected true stress values P to account for the barreling effect during the deformation using (Equation 7). The true stress correction uses the barreling parameter b (Equation 8) where R_m is measured maximum radius after deformation, R_t is the top radius (Equation 13), and R_a is the average radius after deformation (Equation 12). The radius and height for the correction equation are described using (Equation 9) for the radius R and (Equation 10) for the height H. The constant friction used for the stress correction is m calculated using (Equation 11). Once the flow stress is calculated the coefficients can be determined for the inverse hyperbolic sine law using the equations discussed in section 1.3.2.

$$\sigma_{true} = \frac{4F(h_o-\Delta h)}{\pi h_o D_o^2} \qquad \text{Equation 5.}$$

$$\varepsilon_{true} = ln\left[\frac{h_o}{(h_o-\Delta h)}\right] \qquad \text{Equation 6.}$$

$$\frac{P}{\sigma_{flow}} = \frac{8bR}{H}\cdot\left\{\left[\frac{1}{12}+\left(\frac{H}{Rb}\right)^2\right]^{\frac{3}{2}}-\left(\frac{H}{Rb}\right)^3-\frac{me^{-b/2}}{24\sqrt{3}(e^{-b/2}-1)}\right\} \qquad \text{Equation 7.}$$

$$b = 4\times\frac{R_m-R_T}{R_a}\times\frac{h}{h_o-h} \qquad \text{Equation 8.}$$

$$R = R_o exp(-\varepsilon/2) \qquad \text{Equation 9.}$$

$$H = h_o exp(-\varepsilon)$$ Equation 10.

$$m = \frac{(R_a/h)b}{(4/\sqrt{3})-(2b/3\sqrt{3})}$$ Equation 11.

$$R_a = R_o\sqrt{\frac{h_o}{h}}$$ Equation 12.

$$R_t = \sqrt{3 \times \frac{h_o}{h} \times R_o^2 - 2R_m^2}$$ Equation 13.

A.2 Raw Flow Stress Results

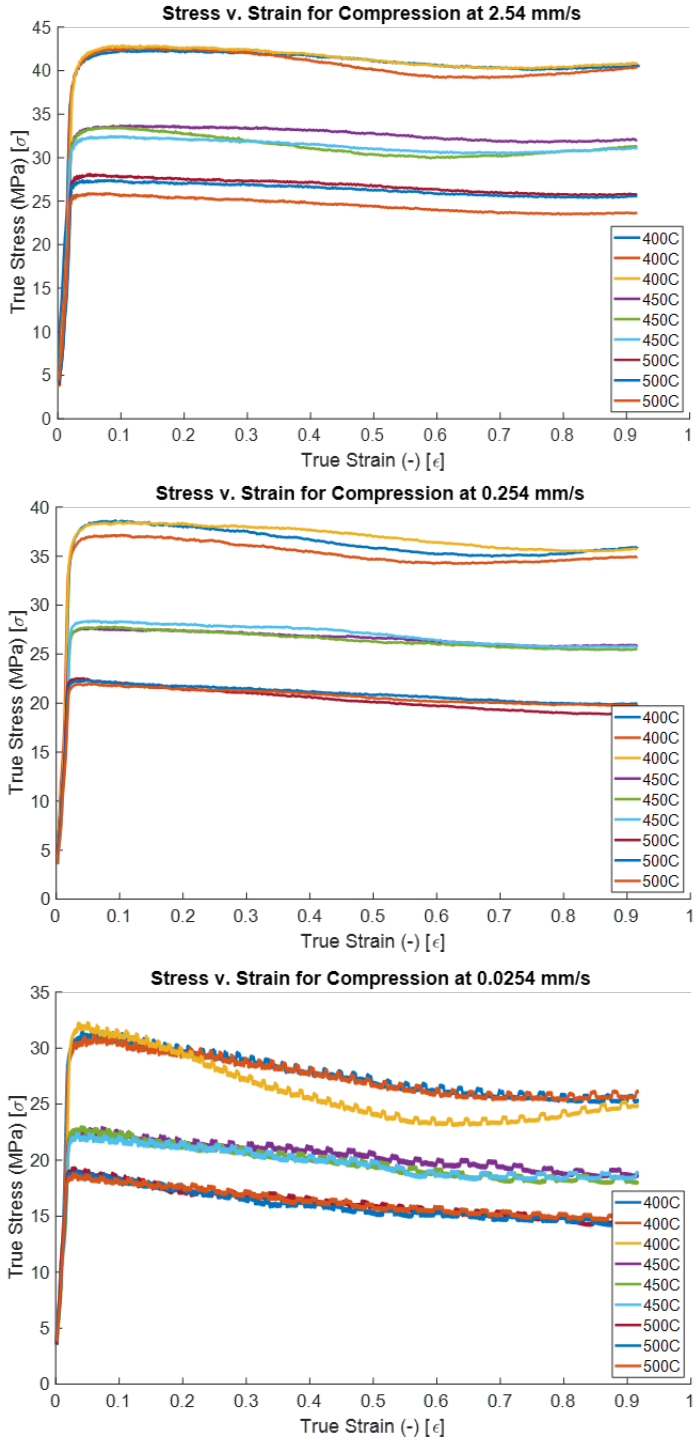

Figure 49. True Stress v. Strain given the 2.54 mm/s, 0.254 mm/s, and 0.0254mm/s test rate condition for the low Mg and low Si alloy at 400°C, 450°C, and 500°C.

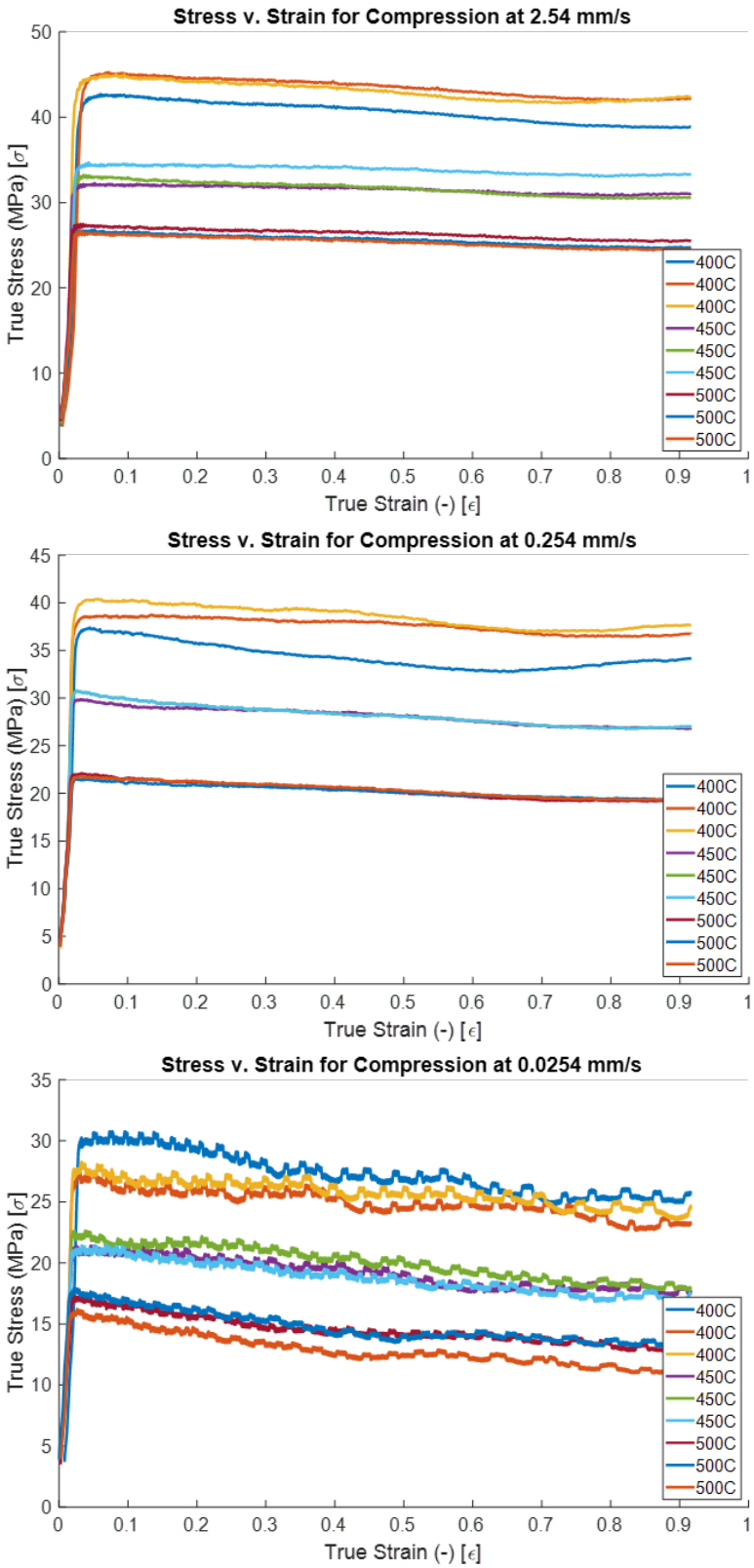

Figure 50. True Stress v. Strain given the 2.54 mm/s, 0.254 mm/s and 0.0254mm/s test rate condition for the high Mg and low Si alloy at 400°C, 450°C, and 500°C.

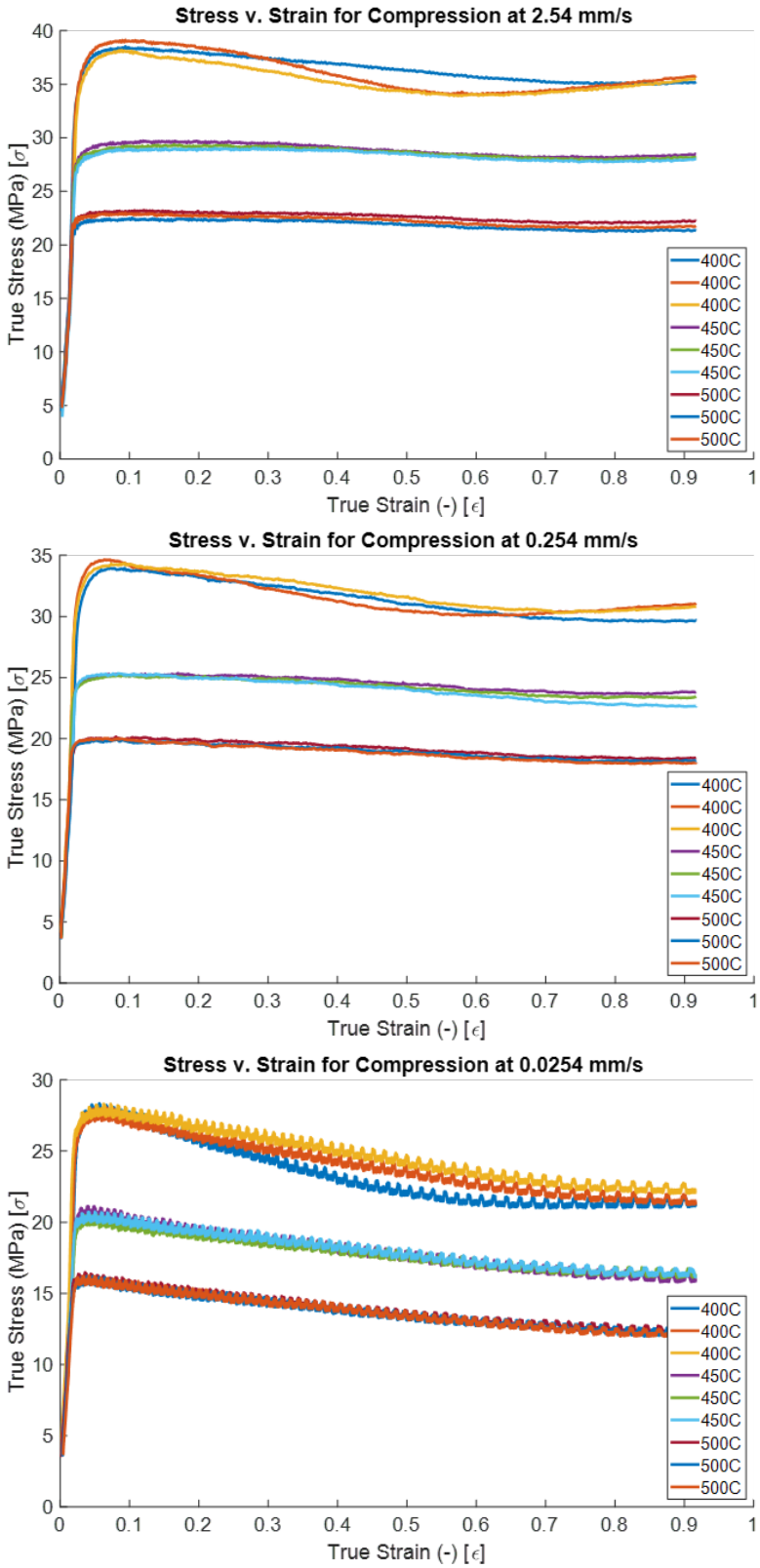

Figure 51. True Stress v. Strain given the 2.54 mm/s, 0.254 mm/s and 0.0254mm/s test rate condition for the low Mg and high Si alloy at 400°C, 450°C, and 500°C.

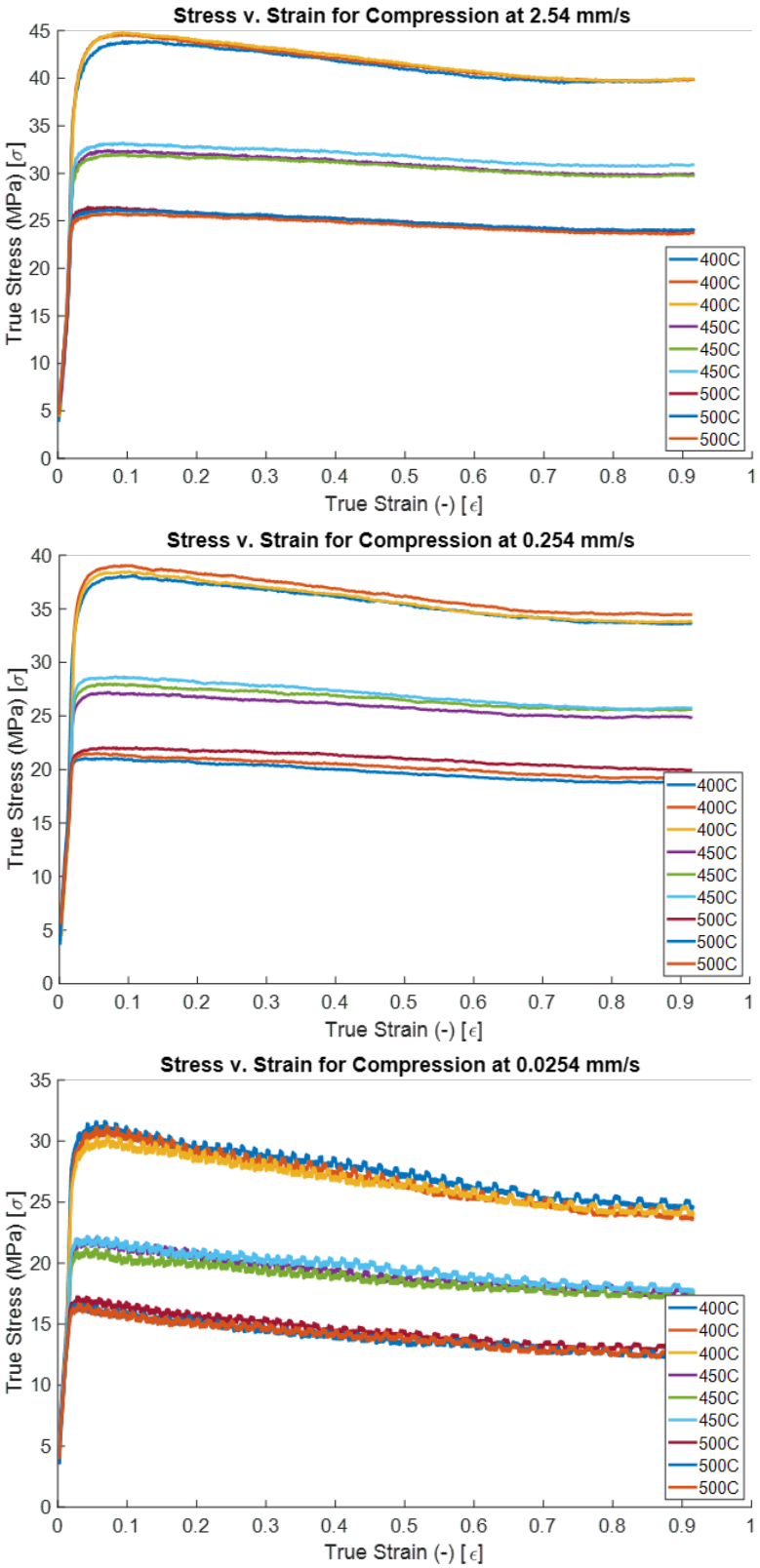

Figure 52. True Stress v. Strain given the 2.54 mm/s, 0.254 mm/s and 0.0254mm/s test rate condition for the high Mg and high Si alloy at 400℃, 450℃, and 500℃.

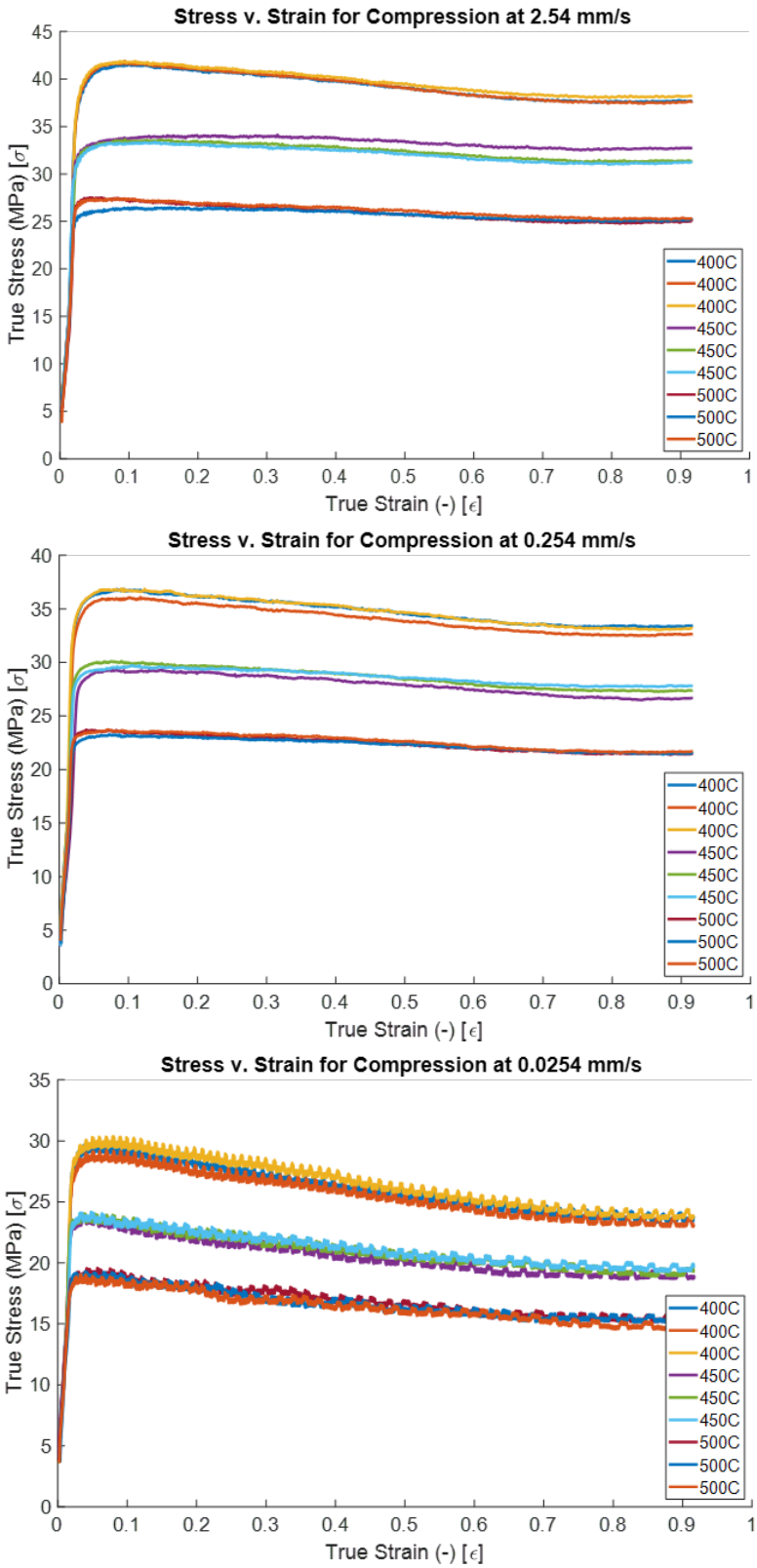

Figure 53. True Stress v. Strain given the 2.54 mm/s, 0.254 mm/s and 0.0254mm/s test rate condition for the medium Mg medium Si alloy at 400°C, 450°C, and 500°C.

A.3 Inverse Hyperbolic Sine Law Fitting

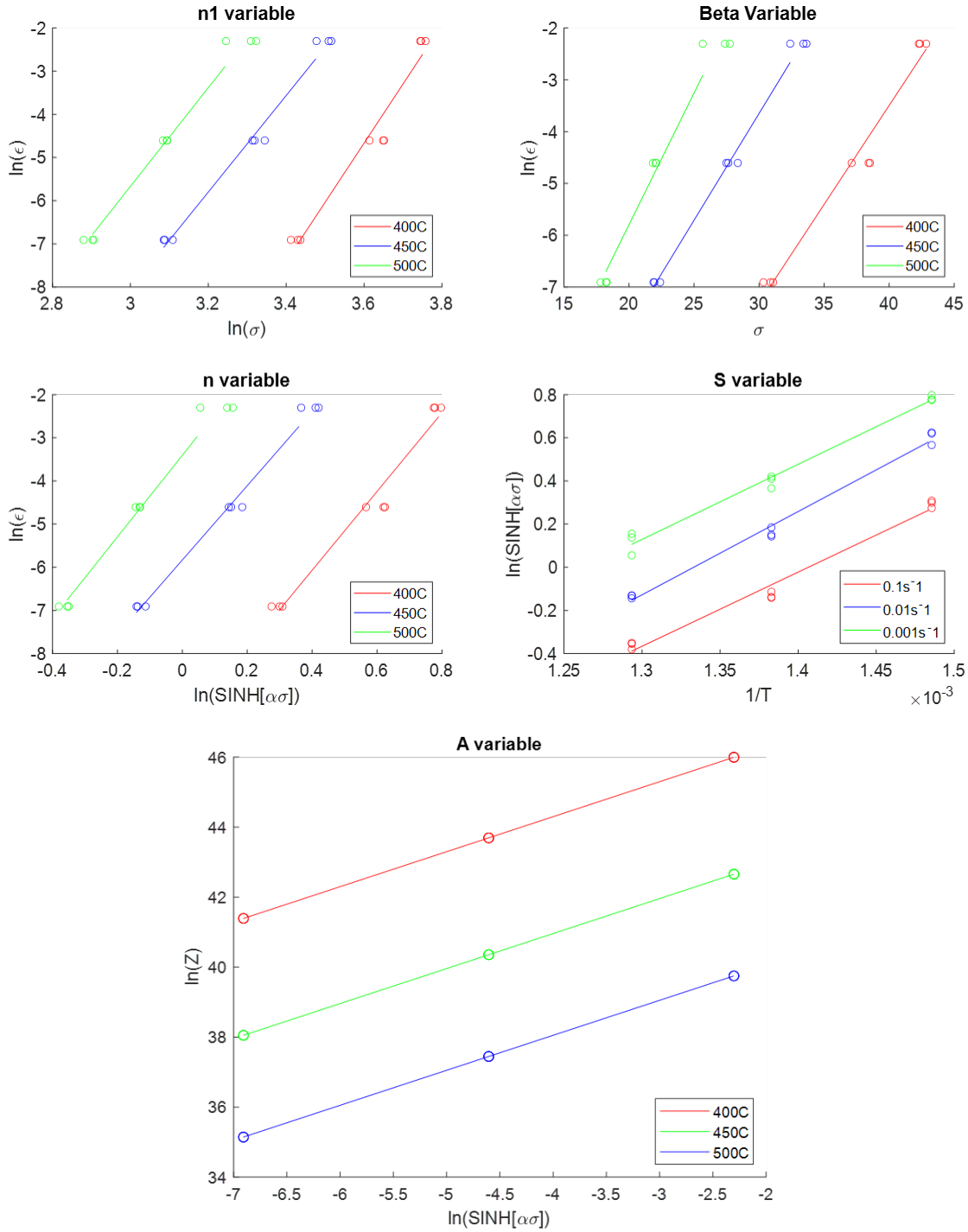

Figure 54. Inverse hyperbolic sine law fitting for n1, n, **β**, S, and A for the low Mg and low Si alloy.

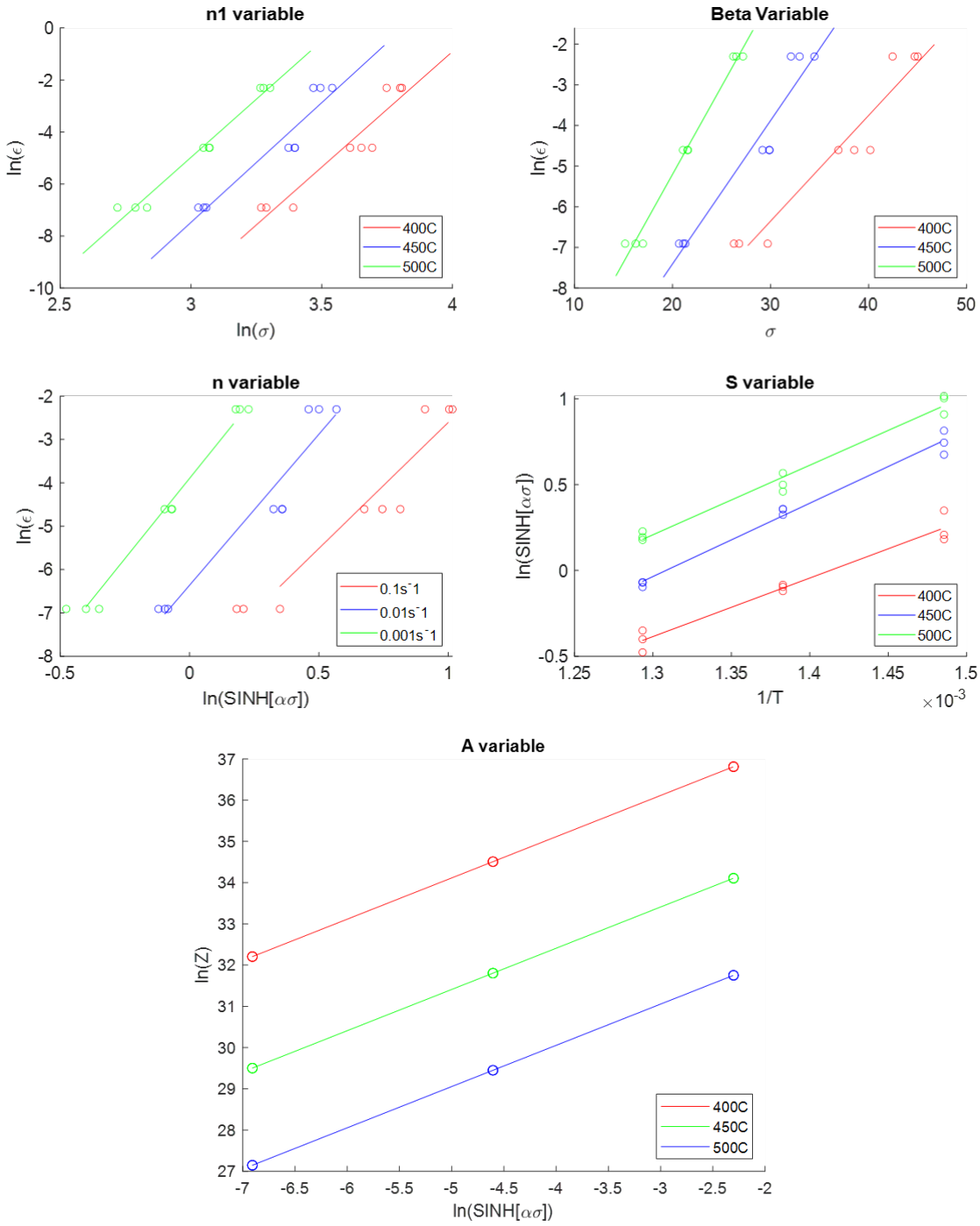

Figure 55. Inverse hyperbolic sine law fitting for n1, n, **β**, S, and A for the high Mg and low Si alloy.

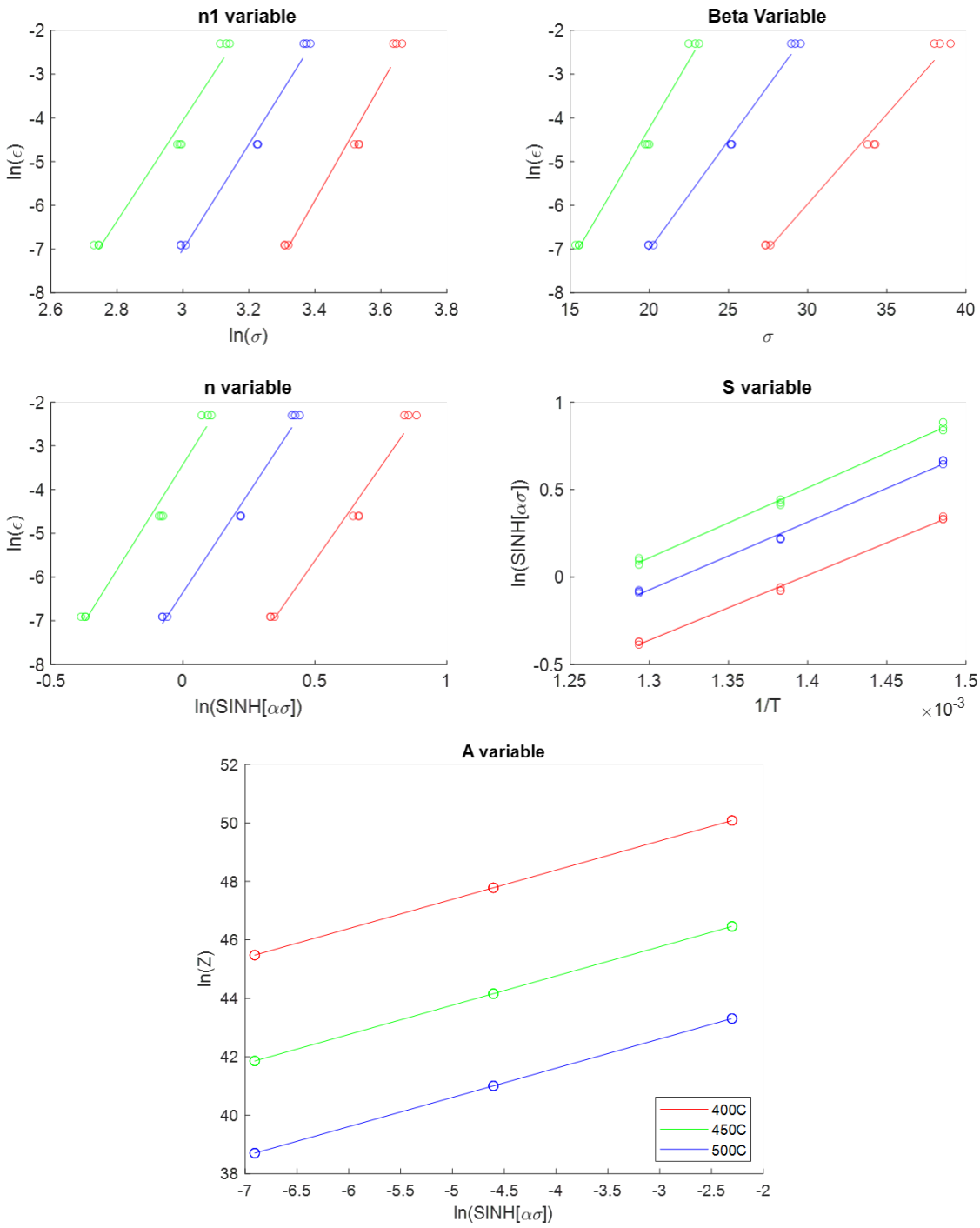

Figure 56. Inverse hyperbolic sine law fitting for n1, n, **β**, S, and A for the low Mg and high Si alloy.

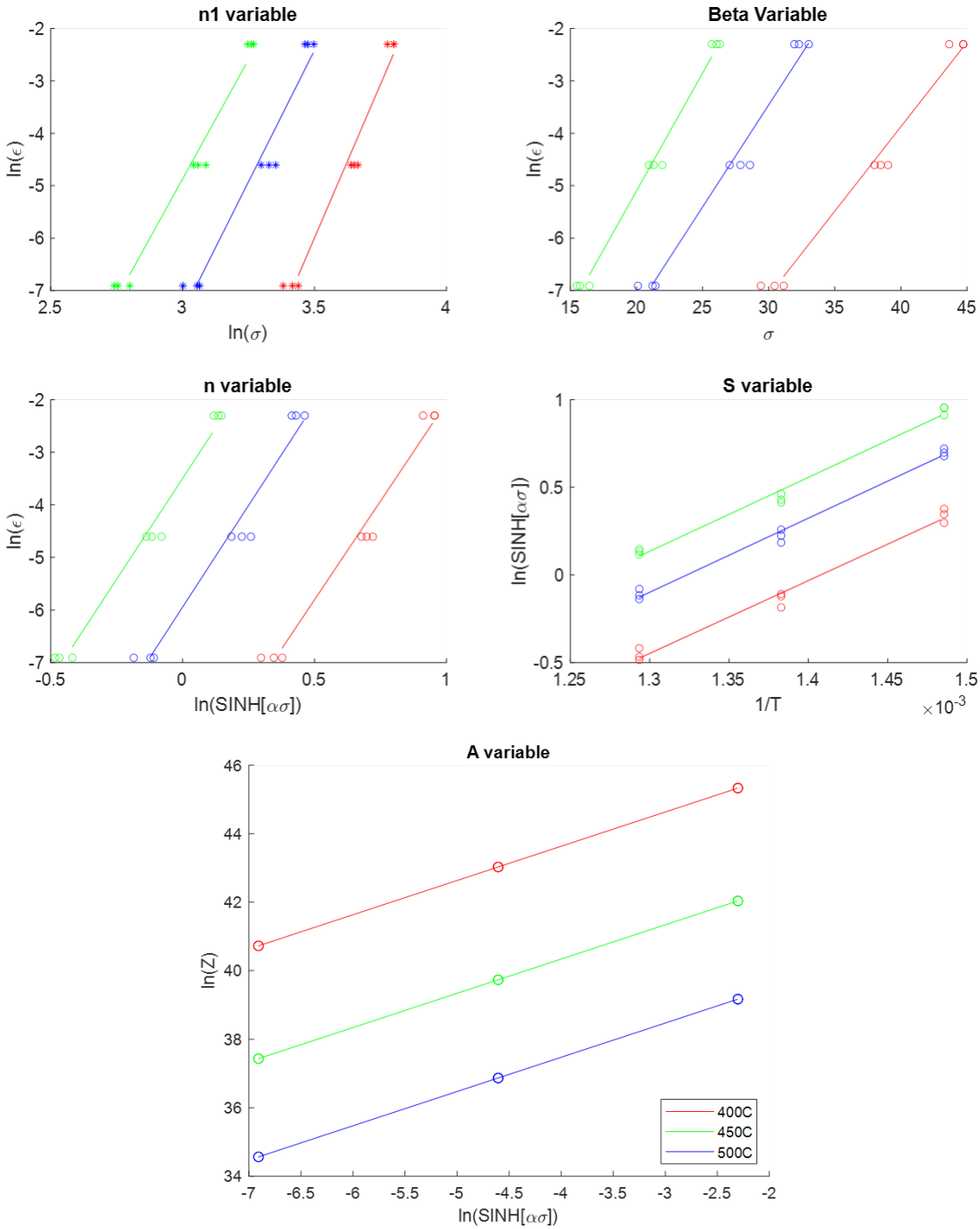

Figure 57. Inverse hyperbolic sine law fitting for n1, n, **β**, S, and A for the high Mg and high Si alloy.

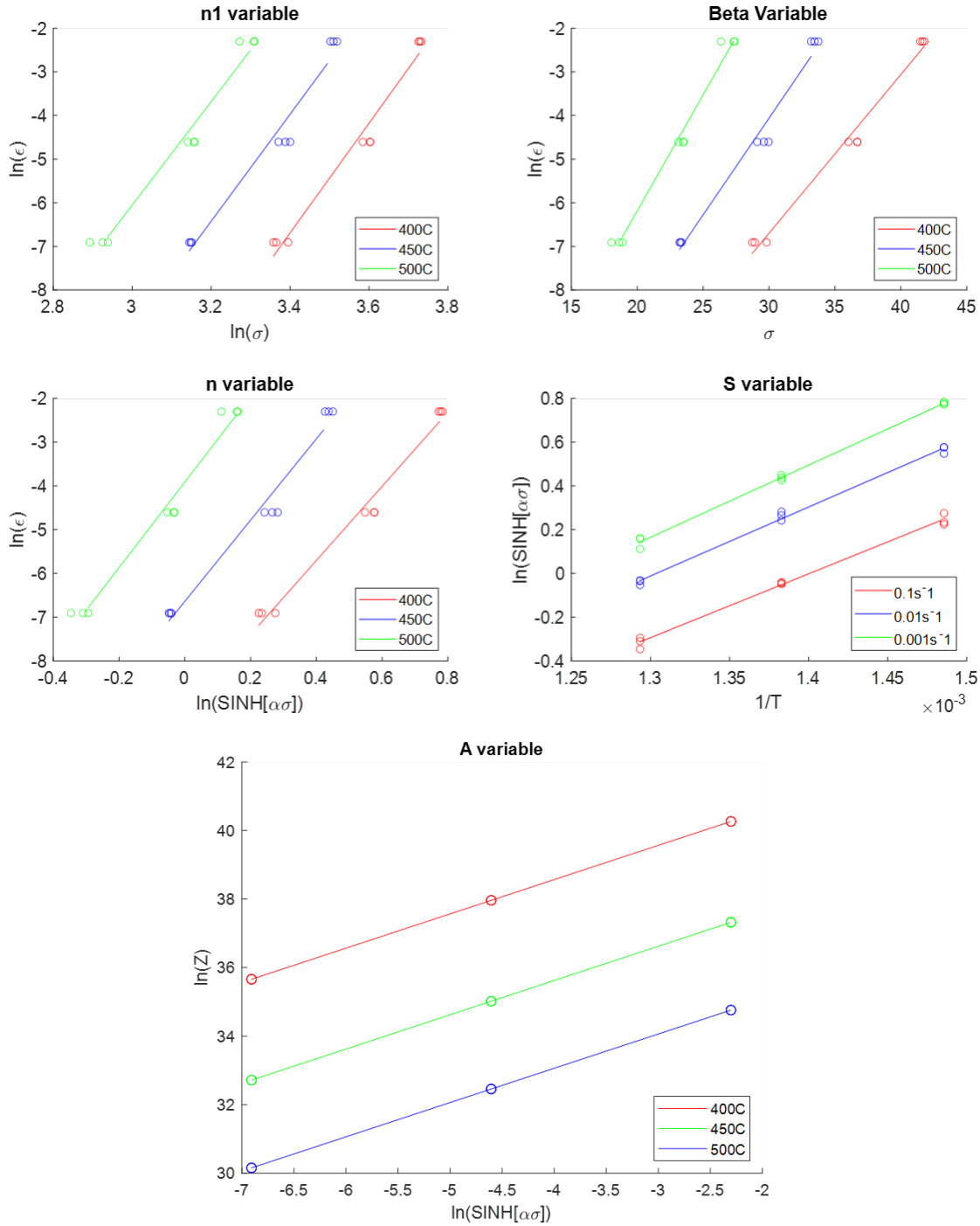

Figure 58. Inverse hyperbolic sine law fitting for n1, n, **β**, S, and A for the medium Mg and medium Si alloy.